

## THE PHYSICS OF TWISTED MAGNETIC TUBES RISING IN A STRATIFIED MEDIUM: TWO-DIMENSIONAL RESULTS

T. EMONET AND F. MORENO-INSERTIS

Instituto de Astrofísica de Canarias, 38200 La Laguna, Tenerife, Spain; temonet@pp.iac.es, fmi@pp.iac.es

Received 1997 June 30; accepted 1997 August 22

### ABSTRACT

The physics of a twisted magnetic flux tube rising in a stratified medium is studied using a numerical magnetohydrodynamic (MHD) code. The problem considered is fully compressible (has no Boussinesq approximation), includes ohmic resistivity, and is two-dimensional, i.e., there is no variation of the variables in the direction of the tube axis. We study a high-plasma  $\beta$ -case with a small ratio of radius to external pressure scale height. The results obtained will therefore be of relevance to understanding the transport of magnetic flux across the solar convection zone.

We confirm that a sufficient twist of the field lines around the tube axis can suppress the conversion of the tube into two vortex rolls. For a tube with a relative density deficit on the order of  $1/\beta$  (the classical Parker buoyancy) and a radius smaller than the pressure scale height ( $R^2 \ll H_p^2$ ), the minimum amount of twist necessary corresponds to an average pitch angle on the order of  $\sin^{-1} [(R/H_p)^{1/2}]$ . The evolution of a tube with this degree of twist is studied in detail, including the initial transient phase, the internal torsional oscillations, and the asymptotic, quasi-stationary phase. During the initial phase, the outermost, weakly magnetized layers of the tube are torn off its main body and endowed with vorticity. They yield a trailing magnetized wake with two vortex rolls. The fraction of the total magnetic flux that is brought to the wake is a function of the initial degree of twist. In the weakly twisted case, most of the initial tube is turned into vortex rolls. With a strong initial twist, the tube rises with only a small deformation and no substantial loss of magnetic flux. The formation of the wake and the loss of flux from the main body of the tube are basically complete after the initial transient phase.

A sharp interface between the tube interior and the external flows is formed at the tube front and sides; this area has the characteristic features of a magnetic boundary layer. Its structure is determined as an equilibrium between ohmic diffusion and field advection through the external flows. It is the site of vorticity generation via the magnetic field during the whole tube evolution.

From the hydrodynamical point of view, this problem constitutes an intermediate case between the rise of air bubbles in water and the motion of a rigid cylinder in an external medium. As with bubbles, the tube is deformable and the outcome of the experiment (the shape of the rising object and the wake) depends on the value of the Weber number. Several structural features obtained in the present simulation are also observed in rising air bubbles, such as a central *tail*, and a *skirt* enveloping the wake. As in rigid cylinders, the boundary layer satisfies a no-slip condition (provided for in the tube by the magnetic field), and secondary rolls are formed at the lateral edges of the moving object.

*Subject headings:* convection — hydrodynamics — methods: numerical — MHD — Sun: interior — Sun: magnetic fields

### 1. INTRODUCTION

The rise of magnetic flux from the deep levels of the solar convection zone to the photosphere is a complex phenomenon involving many different magnetic and hydrodynamical processes. Particular attention has been devoted in the past 20 years to the time evolution of a single buoyant magnetic flux tube considered as a one-dimensional object (Moreno-Insertis 1983; 1986; Choudhuri 1989; D'Silva & Choudhuri 1993; Fan, Fisher, & DeLuca 1993; Fan, Fisher, & McClymont 1994; Caligari et al. 1995. Further references and a recent review can be found in Moreno-Insertis 1997a). These calculations incorporate several aspects of the basic physics of the rise of the magnetic tubes (buoyancy, magnetic and rotational forces, external stratification, etc.). They have been successful in predicting morphological and kinematic features of the resulting active regions that have been observed at the surface of the Sun.

Yet, the assumption of one-dimensionality in the magnetic region is certainly a drastic simplification. From laboratory and numerical experiments in different contexts, we know that there are complicated hydrodynamical and

magnetic structure within and outside of a tubular object that is moving with respect to the surrounding fluid. The one-dimensional numerical models mentioned above, in particular, do not include two ingredients that turn out to be fundamental in studying the rise of buoyant magnetized plasma regions, i.e., the vorticity of the velocity field and the twist of the field lines around the main axis of the tube.

Vorticity and transverse field components may be crucial for the formation of the tubes in the first place (Cattaneo & Hughes 1988; Cattaneo, Chiueh, & Hughes 1990; Matthews, Hughes, & Proctor 1995). They also play a central role in the time evolution of the rising magnetic region. A clear warning in this sense came from the work of Schüssler (1979), who showed how the cross section of a straight, buoyant magnetic tube initially at the same temperature as its surroundings develops an *umbrella* shape (two side lobes connected on their upper side by an arch). The side lobes rotate in opposite directions around a horizontal axis, each thus constituting a vortex tube; they finally detach from each other and from the arch above them. The whole process occurs at the beginning of the rise,

namely, before the tube has risen across a height equivalent to a few times its own diameter. The physics involved has been considered in detail by Longcope, Fisher, & Arendt (1996). These authors have studied the Boussinesq problem, including untwisted and very weakly twisted magnetic tubes. They clearly show how the two rotating side lobes, when detached from the rest, are subjected to a downward-pointing lift force, as a result of their flow being non-circulation free. In the end, the lift cancels the buoyancy force, this being the reason for their horizontal asymptotic motion. If this were a universal mechanism operating on all rising magnetic flux tubes, then magnetic buoyancy should no longer be considered an efficient mechanism for bringing magnetic flux to the photosphere.

In the present paper, we consider in detail the more general case of a buoyant magnetic flux tube with an arbitrary initial twist of the field lines (but still horizontal and with uniform values of all variables along the direction of the axis). The transverse magnetic field (i.e., the component of the field vector normal to the tube axis) imparts a certain rigidity to the tube cross section. If it is strong enough, it can prevent the conversion of the tube into a vortex tube pair. The minimum amount of twist necessary for this corresponds to an average pitch angle on the order of  $\sin^{-1} [(R/H_p \beta/2 |\Delta\rho/\rho|)^{1/2}]$ , with  $R$  being the tube radius,  $H_p$  the external pressure scale height, and  $\Delta\rho$  the density difference between the tube and its surroundings (see § 3.1). This approximate criterion is indeed fulfilled by magnetic tubes with classical Parker magnetic buoyancy, as shown in a preliminary presentation of this paper (Moreno-Insertis & Emonet 1996). In the present article, we explore in more detail the physics involved in that process, discussing a number of MHD processes occurring inside the tube, in the boundary layer, at its periphery, and in the trailing wake. We also show how the results of Schüssler (1979) and Longcope et al. (1996) can be seen as limiting cases in which the trailing wake in fact engulfs most of the original rising tube. The pitch angle just mentioned thus signals the borderline between the weak and strong twist regimes; a buoyant tube with an initial twist above this level rises without being strongly deformed and is followed by a wake containing only a small fraction of the initial total magnetic flux.

In addition to the work of Moreno-Insertis & Emonet (1996), there is another paper in the recent literature dealing with a related subject (Cargill et al. 1996). These authors have studied the interaction of a twisted tube with a magnetized medium in the absence of gravity when the tube is subjected to an ad hoc, spatially uniform acceleration. Special emphasis was put on the reconnection of the ambient magnetic field with the tube's own. Neither buoyancy, stratification, nor different degrees of twist were studied in that article. Two further papers, submitted simultaneously with the present one, deal with the rise of buoyant twisted magnetic tubes (Fan, Zweibel, & Lantz 1997; Hughes, Falle, & Joarder 1998). The first authors, in particular, study the interaction between tubes rising in pairs. The results of both papers concerning the rise of single tubes are in general agreement with those of Moreno-Insertis & Emonet (1996).

The layout of this article is as follows. After a brief presentation of the equations and numerical procedure in § 2, the basic features of the physical problem are considered in § 3. This includes the main parameters and a discussion of

the amount of twist necessary to prevent the deformation of the tube and its conversion into vortex rolls. In § 4, the simulation of the rise of a tube with that amount of twist is presented. In particular, the initial acceleration phase, the internal torsional oscillations, and the later asymptotic phase are discussed. Section 5 deals with the structure of the magnetic boundary layer around the tube, and § 6 examines the trailing wake. Finally, the transition between the twisted and untwisted case is explained in § 7. A general discussion follows in § 8.

## 2. EQUATIONS AND NUMERICAL PROCEDURE

### 2.1. Equations

Our medium is an ideal compressible and stratified gas governed by the general equations of magnetohydrodynamics (MHD), including Ohmic diffusion:

$$\frac{D\rho}{Dt} = -\rho \nabla \cdot \mathbf{v}, \quad (1)$$

$$\rho \frac{D\mathbf{v}}{Dt} = -\nabla p + \frac{1}{4\pi} (\nabla \times \mathbf{B}) \times \mathbf{B} + \rho \mathbf{g}, \quad (2)$$

$$\frac{\partial \mathbf{B}}{\partial t} = \nabla \times (\mathbf{v} \times \mathbf{B}) + \eta \Delta \mathbf{B}, \quad (3)$$

$$\rho \frac{De}{Dt} = -p \nabla \cdot \mathbf{v} + \frac{\eta}{4\pi} (\nabla \times \mathbf{B})^2, \quad (4)$$

where  $e$  is the internal energy per unit mass and  $\eta$  is the ohmic diffusivity, which is assumed to be constant. All other symbols have their customary meaning. Cartesian coordinates  $(x, y, z)$  are adopted, so that the  $z$ -direction is anti-parallel to  $\mathbf{g}$ . In this paper, we consider a two-dimensional problem; i.e., we assume that there are no variations of the physical variables along the  $y$ -axis ( $\partial/\partial y \equiv 0$ ), although  $B_y$  and  $v_y$  are generally nonzero.

Equations (1)–(4) are cast in their conservative form and solved with a code written by Shibata 1983. This is based on a modified Lax-Wendroff scheme (Rubin & Burstein 1967) and stabilized with artificial viscosity, as described by Richtmyer & Morton (1967). The inclusion of physical resistivity in our equations and the absence of any shock phenomena in the solutions permit us to minimize the use of the artificial viscosity. The latter is restricted, in any case, to regions of very steep gradients only.

This code has been repeatedly tested and used for two-dimensional simulations of the outbreak of the magnetic field at the surface of the Sun by Shibata and collaborators (see, e.g., Shibata 1983; Shibata et al. 1989; Kaisig et al. 1990). In addition, we have successfully run several tests for our problem, checking for the convergence of the code as well as for conservation of mass, energy, and magnetic flux in the box.

In this article, we only consider a case with left-right symmetry about a vertical plane containing the tube axis. For each half of the tube, we use a numerical grid of 300 points in the horizontal direction and 700 points in the vertical (although in the figures presented here, only a small fraction of the box is shown). In the following discussion, the results are given in dimensionless form, using as units the background density, pressure scale height, and Alfvén speed calculated at the center of the tube at time  $t = 0$ .

## 2.2. Initial Conditions

The initial condition consists of an unperturbed background atmosphere with pressure  $p_e$  and density  $\rho_e$ , and, superimposed, a perturbation associated with a magnetic flux tube. To avoid any confusion arising from pseudo-convective effects, the background atmosphere is adiabatically stratified. It spans vertically 80% of the pressure scale height at the bottom of the box. The pressure contrast between the top and bottom is 2.6. The density contrast is 1.8.

After inclusion of the magnetic tube, the resulting system satisfies the following simple condition:  $-\nabla \Delta p + \mathbf{J}/c \times \mathbf{B} = 0$ , with  $\Delta p \equiv p - p_e$  being the pressure excess as compared to the background stratification,  $\mathbf{J}$  being the electric current density, and  $c$  being the speed of light. In the absence of gravity, this would be a perfect equilibrium condition. The density profile in the magnetic region is determined by assuming that the entropy in the tube is constant and equal to the unperturbed value in the atmosphere. The tube at time  $t = 0$  is thus buoyant ( $\rho < \rho_e$ ) and fulfills the condition

$$\frac{\Delta \rho}{\rho} \equiv \frac{\rho - \rho_e}{\rho} \simeq -\frac{1}{\gamma \beta} \quad (5)$$

to first order in  $1/\beta$ , with  $\gamma$  being the specific heat ratio. This case is intermediate between the two extreme possibilities of full thermal equilibrium, i.e.,  $T = T_e$  (which would be a factor  $\gamma$  more buoyant), and the case of a tube with  $\rho = \rho_e$ . The evolution presented here is qualitatively very similar to the first case, while it deviates in important respects from the second.

In this paper we will deal with a number of different magnetic field profiles at time  $t = 0$ . The longitudinal field  $B_l = B_y$  will be taken to have a Gaussian profile,

$$B_l(t = 0) \propto \exp(-r^2/R^2). \quad (6)$$

The transverse field  $B_t(t = 0)$  is chosen to be purely azimuthal; calling  $r$  and  $\phi$  the polar coordinates around the tube center, we have  $\mathbf{B}_t(t = 0) = B_\phi \mathbf{e}_\phi$ . For  $B_\phi$ , we will choose distributions such that the pitch angle  $\Psi$ ,

$$\Psi \equiv \text{atan} \left( \frac{B_\phi}{B_l} \right), \quad (7)$$

adopts an asymptotically flat profile,

$$B_\phi \propto B_l \frac{ar^n}{ar^n + R^n}, \quad (8)$$

or, alternatively, an exponentially decaying one,

$$B_\phi \propto B_l \left( \frac{1}{\sqrt{n}} \frac{r}{R} \right)^n \exp \left( -\frac{r^2}{R^2} + \frac{n}{2} \right). \quad (9)$$

The choice of  $n$  determines the *rigidity* of the tube center. In this paper, we consider the case  $n = 3$  and  $a = 0.9$ . As we will see, both profiles given by equations (8) and (9) yield basically the same time evolution (§ 5.1). As explained in the discussion, we have also run some tests with flat, top-hat magnetic profiles (§ 8.1).

## 2.3. Boundary Conditions

The side and bottom boundaries are closed lids. A closed boundary at the top of the box must be avoided for two

reasons: (1) the sound waves generated by the tube in the external medium must be able to leave the box and (2) the rise of the tube should not be unduly braked through excess pressure from a closed boundary at the top. An ideal *free* boundary should be transparent for the outgoing disturbances and should not introduce disturbances through incoming waves. In the present calculations, we achieve this by introducing a *fiducial layer* (Nordlund & Stein 1990) well above the upper boundary of the box. At each time step, the pressure in the fiducial layer is calculated by assuming that each point in it is in static equilibrium with respect to the point on the boundary of the box lying directly below it; the densities are then obtained via the constant background entropy, and the velocity is set to zero in the fiducial layer. The net mass flux across the boundary is not necessarily zero. However, the total mass of the box only varies by a maximum factor of  $10^{-6}$  during each single run.

## 3. THE PHYSICAL PROBLEM: PARAMETERS GOVERNING THE EVOLUTION

The present physical problem is characterized by four basic dimensionless input parameters: (1) the thickness of the tube in units of the local pressure scale height,  $\tilde{R} \equiv R/H_p$ ; (2) the plasma  $\beta$  at the center of the tube,  $\beta_0$ ; (3) the ratio between the transverse and the longitudinal components of the field, as measured by, e.g., the pitch angle at a representative position of the tube,  $\Psi_{\text{mt}}$ , to be specified; (4) the ohmic diffusivity  $\eta$  in terms of, e.g.,  $v_A H_p$ , with  $v_A$  being the Alfvén speed,  $\tilde{\eta} \equiv \eta/(v_A H_p)$ .

These parameters determine the properties of the initial magnetic tube and are independent of the velocity of the flow that develops along time. However, in this problem there is a characteristic value for the flow velocity, namely, the terminal speed of rise,  $v_{\text{term}}$ , given by the dynamical equilibrium between buoyancy and aerodynamic drag:

$$v_{\text{term}}^2 \sim \frac{\pi}{\gamma} \frac{\tilde{R}}{C_D} \frac{\Delta \rho}{\rho} c_s^2, \quad (10)$$

where  $C_D$  is the customary drag coefficient,  $C_D \sim O(1)$ , and  $c_s$  is the sound speed. Hence, the customary velocity-related parameters, such as the Mach number, the Reynolds number, and the magnetic Weber number, can be immediately obtained as functions of the foregoing input parameters. For instance, using equation (5), we obtain that the Mach number must be on the order of  $M^2 = O(\tilde{R}/\beta_0)$ . As a result, we expect the rise to be very subsonic and, assuming  $\tilde{R} \ll 1$ , sub-Alfvénic as well. This latter condition can be violated for tubes rising to higher levels of the convection zone.

The rest of this section is devoted to a discussion of the values expected for the most important parameters in this problem.

### 3.1. The Amount of Twist and the Deformation of the Tube

The central parameter for the present paper is the twist of the tube as measured by the pitch angle of the field lines,  $\Psi$ . The values of this parameter of interest for our calculation are those for which the transverse component of the field,  $B_t$ , is able to suppress the conversion of the tube into a pair of vortex rolls. In the following section we study different agents that tend to deform the tube. We come to the conclusion that the minimum value of  $B_t$  necessary to counteract them is the same for all.

### 3.1.1. Differential Buoyancy and Pressure Fluctuations along the Boundary

The tube of the initial condition explained in § 2.2 is increasingly buoyant toward its center. Thus, the central regions rise faster than the periphery; the upper layers of the tube are thereby compressed, while those located below the center are expanded. The magnetic field lines are deformed by this process; the transverse field, in particular, exerts an increasing resistance against further deformation. One can calculate the minimum transverse field that can effectively withstand (and reverse) the buoyant deformation (Emonet & Moreno-Insertis 1996). At this point, it is sufficient to obtain an order of magnitude estimate for it that can serve as a guide for the rest of the paper. This can be easily done for tubes with smooth distributions, such as given in equations (6) and (8) or (9), and satisfying  $R^2 \ll H_p^2$ . The resulting criterion is best expressed in terms of the pitch angle calculated at the position of the maximum of the transverse field,  $\Psi_{\text{mt}}$ ; it reads:

$$\sin \Psi_{\text{mt}} \equiv \left( \frac{B_t}{B} \right)_{\text{mt}} \gtrsim \tilde{R}^{1/2} \left( \left| \frac{\Delta\rho}{\rho} \right|_0 \frac{\beta_0}{2} \right)^{1/2}. \quad (11)$$

For tubes with initial conditions as given in § 2.2, this approximate criterion should hold to within about a factor of 2. A more precise condition involving the detailed buoyancy distribution in the tube can be obtained by studying the magnetostatic equilibrium of a horizontal twisted tube with a nonhomogeneous buoyancy distribution in the limit  $R^2 \ll H_p^2$  (Emonet & Moreno-Insertis 1996). It can be shown (see their eqs. [44] and [49]) that for the deformation of the tube to remain small, the radial profile of the pitch angle,  $\Psi(r)$ , must satisfy

$$\sin \Psi(r) \gtrsim \left( \frac{r}{H_p} \right)^{1/2} \left[ \left| \frac{\Delta\rho(r) - \langle \Delta\rho \rangle(r)}{\rho(r)} \right| \beta(r) \right]^{1/2}, \quad (12)$$

where  $\langle f \rangle(r)$  is the radial average of  $f$  between the radii 0 and  $r$ . At each radius  $r$ , the deformation of the magnetic field is directly related to  $\Delta\rho(r) - \langle \Delta\rho \rangle(r)$ , i.e., to the differential buoyancy at that radius.

The threshold due to the differential buoyancy (eq. [11] or eq. [12]), however, cannot be the only criterion of interest for our problem. In fact, even a uniformly buoyant tube, if untwisted, is subjected to deformation and conversion into vortex rolls. One deforming agent independent of the initial differential buoyancy is the pressure profile (i.e., the pressure fluctuations,  $p_{\text{ef}}$ , above the background stratification) built by the external flow around the boundary of the tube (Emonet & Moreno-Insertis 1996); a simple criterion for the resistance of the tube against those fluctuations is

$$\frac{8\pi |p_{\text{ef}}|}{B_t^2} \lesssim 1. \quad (13)$$

Now,  $p_{\text{ef}}$  is itself on the order of the ram pressure of the external flow relative to the tube. Thus, it is no higher than about  $\rho v_{\text{term}}^2/2$ . Substituting from equation (10), we obtain again a criterion as in equation (11).

### 3.1.2. Vorticity Generation

Given the central role of the vorticity in the present problem, it is adequate to understand the minimum condition given in equation (11) in terms of vorticity generation. The time evolution of the longitudinal component of the

vorticity,  $\omega_r$ , is governed by the following equation:

$$\rho \frac{D}{Dt} \left( \frac{\omega_l}{\rho} \right) = \nabla \left( \frac{\Delta\rho}{\rho} \right) \times g + \frac{\nabla \times F_{\text{Lt}}}{\rho} + \nabla \left( \frac{1}{\rho} \right) \times \left[ -\nabla \left( \Delta p + \frac{B_t^2}{8\pi} \right) + F_{\text{Lt}} \right]. \quad (14)$$

$F_{\text{Lt}}$  represents the projection of the Lorentz force on the transverse plane ( $x, z$ ). For definiteness, when speaking about the sign of the vorticity in the rest of this section, we refer to the right half of the tube only.

An issue in this section is the generation of vorticity in the main body of the tube (the vorticity in the tube periphery is discussed in § 5.2). The first term on the right-hand side of equation (14) is the counterpart in terms of vorticity of the gravitational torque: it produces *positive* vorticity because  $\nabla(\Delta\rho/\rho)$  points outward. The second term on the right-hand side of equation (14) represents the effect of  $B_t$  and can be rewritten as:

$$\frac{\nabla \times F_{\text{Lt}}}{\rho} = \frac{(B_t \cdot \nabla) J_l}{c\rho}, \quad (15)$$

with  $J_l$  being the longitudinal component of the electric current density. At the beginning of the run, the longitudinal current is axisymmetric, so that  $\nabla \times F_{\text{Lt}}$  is zero. As soon as the tube center begins to rise relative to the periphery, the longitudinal current is enhanced in the upper half and diminishes in the lower half of the tube. According to equation (15), this produces *negative* vorticity in the interior of the tube, i.e., it tends to counteract the effect of the gravitational torque. By setting these two terms to be equal, we obtain a criterion for the minimum transverse magnetic field that can effectively oppose the initial deformation of the tube; the result is, again, equation (11). For the problem we consider here, the last term of the vorticity equation (14) is  $O(\Delta\rho/\rho + L/\gamma H_p)$  smaller than the other two terms and is therefore not of primary interest here ( $L$  represents a local characteristic length for the transverse magnetic field, e.g., the radius of the tube or the thickness of the tube boundary).

Criteria equivalent to equation (11) can also be obtained through other physical considerations. For instance, Tsinganos (1980) obtained a similar threshold for  $\Psi$  by calculating the stability of the tube against splitting due to the development of Rayleigh-Taylor and Kelvin-Helmholtz instabilities at its apex.

## 3.2. Other Parameters

### 3.2.1. Plasma $\beta$ and Tube Radius

The choice of values for the parameters  $\beta_0$  and  $\tilde{R}$  must be guided both by (astro)physical insight and feasibility of the numerical calculation.  $\beta_0$  is expected to be very high in the solar interior, perhaps  $O(10^5)$  for the magnetic tubes at the bottom of the convection zone. The Courant condition for the numerical code, however, sets a stringent upper limit to the value of  $\beta_0$  that we can use. Using equation (10), we can calculate the number of time steps necessary for our tube to cross the whole integration box,  $n_t$ , as

$$n_t \gtrsim n_z \left( \frac{\beta_0}{\tilde{R}} \right)^{1/2}, \quad (16)$$

with  $n_z$  being the total number of cells in the vertical direction. A trade-off between field intensity and the magnetic flux of the tube is then necessary. As a compromise, we have chosen  $\beta_0 = 10^3$  and  $\tilde{R} = 3.7 \times 10^{-2}$ . This should be sufficient to understand qualitatively the flows in and around the tubes with the field strength and flux expected in the progenitors of active regions.

### 3.2.2. The Magnetic Reynolds Number

The magnetic Reynolds number can be defined in this problem in terms of the terminal speed of rise and the tube radius. Its order of magnitude is thus given by  $\text{Re}_m = O(\tilde{R}^{3/2}/\tilde{\eta})$ . The choice of a value for this parameter must be guided primarily by numerical criteria: large magnetic field gradients develop in the tube along the evolution, especially at its upper rim. We have chosen the ohmic diffusivity so that the resulting value of  $\text{Re}_m$  is a few times  $10^2$ . This yields good numerical performance, but causes some unwanted diffusion of the field outward from the tube. A measure for this diffusion can be obtained from the  $y$ -component of Walen's equation, obtained by combining the continuity and induction equations (1) and (3):

$$\frac{D}{Dt} \left( \frac{B_l}{\rho} \right) = \left( \frac{\mathbf{B}}{\rho} \cdot \nabla \right) v^y + \frac{\eta}{\rho} \Delta B_l. \quad (17)$$

In the central region of the tube, the variation in  $B_l/\rho$  is basically a result of diffusion. The calculations presented in the following discussion are not diffusion dominated (as expected from the high  $\text{Re}_m$ ), in the sense that the decrease of this quantity is small in the tube center during the time period shown in the figures. This can also be checked through an order of magnitude estimate; the diffusion term in equation (17) for the initial Gaussian distribution can be compared to the rate of change of the field (left-hand side of the same equation) imposed by the rise of the tube. The ratio between them is  $(\text{Re}_m \tilde{R})^{-1}$ , which is  $O(10^{-1})$  in the present case.

### 3.2.3. The Weber Number

In the hydrodynamical literature on air bubbles, the Weber number is used to measure the relative importance of the inertial forces of the flow to the surface tension at the boundary of the bubble (e.g., Ryskin & Leal 1984b). The role of surface tension is played in our case by the jump in magnetic tension of the transverse component at the boundary of the tube. Hence, we define the magnetic Weber number as

$$\text{We} \equiv \frac{v^2 \rho}{B_t^2 / (4\pi)}. \quad (18)$$

Inserting for  $v$  the terminal speed, we easily obtain  $\text{We} = \tilde{R} \beta_0 |\Delta \rho / \rho|_0 / (2 \sin^2 \Psi_{\text{mt}})$ . The condition on the minimum pitch angle to avoid splitting of the tube, given in equation (11), can thus be reformulated as the condition that the Weber number be at most of order one,  $\text{We} \lesssim 1$ .

## 4. THE RISE OF A TWISTED TUBE IN A MODERATELY STRATIFIED ENVIRONMENT: A REPRESENTATIVE CASE

The critical value of the pitch angle parameter  $\Psi_{\text{mt}}$  obtained by substituting in equation (11) the chosen values of  $\beta_0$ ,  $\tilde{R}$ , and  $\Delta \rho / \rho$  is  $6^\circ$ . In the present section, we describe some major features of the rise of a tube with a pitch angle  $\Psi_{\text{mt}}$  close to that value,  $\Psi_{\text{mt}} = 7^\circ$ . The time evolution is

illustrated in Figure 1, which shows a fraction of the integration box used (30% and 70% of the box in the horizontal and vertical directions, respectively). In § 7, we compare the results for flux tubes with different values of the initial  $\Psi_{\text{mt}}$ .

### 4.1. The Initial Acceleration Phase

In the absence of external flows to keep it in place, the tube lacks equilibrium globally and starts to rise, at the same time sending out sound waves all across the box. The initial global acceleration is basically *free-fall*, i.e.,  $(g/i)(\overline{\Delta \rho / \rho})$ , with an overbar indicating average values in the tube and  $i$  standing for the enhanced inertia factor, which turns out to be 2 (see § 4.3.1).

Superimposed on the global rise, different kinds of motions within and around the tube take place that tend to deform its initial axisymmetric shape (Fig. 1, *upper row*). One of these is the faster rise of the tube center compared to the periphery as a result of the differential buoyancy (§ 3.1.1). As a consequence of this, the magnetic tension associated with the transverse field builds up at the tube front; the relative motion of the tube center is thus stopped and reversed. A vertical oscillation of the tube center ensues within the tube's cross section. The compression/expansion in the upper/lower half of the tube, together with the internal oscillations, are clearly visible in Figure 2, where we have plotted the position as a function of time for several Lagrange markers located along the vertical symmetry axis of the tube.

Simultaneously with the processes just explained, the external matter slides around the tube and *drags* toward the rear the outermost tube layers, where the magnetic field is too weak to oppose any important Lorentz force. The field is thus stretched all along the boundary (§ 5). Vorticity is being generated in the matter being dragged; as a result, two magnetized vortex rolls are created that trail the tube motion (Fig. 1, *third panel*). The main body of the tube thereby loses about 30% of its original magnetic flux. This figure sensitively depends on the initial pitch angle (§ 7). Given the sign of the vorticity, the matter between the rolls is moving upward with respect to the back of the tube. A pressure excess appears at the upper end of the intervortex space, directly below the lowermost tube layers.

### 4.2. Torsional Oscillations of the Tube Interior

The vertical oscillations of the tube center are in fact part of a torsional oscillation in which most of the tube interior is taking part (Fig. 3). The torsional oscillation has left-right symmetry; each tube half is rotating back and forth around a horizontal axis offset by a fraction of  $R$  from the midplane. The energy of this oscillation is being radiated away from the tube via pressure forces; it is also damped through the diffusion (physical and numerical) present in the code. Thus, it slowly decreases in amplitude. The frequency of these oscillations is on the order of  $\omega_{\text{tors}} = O[v_{\text{At}} / (2\pi R)]$ . Hence, one expects a few torsional oscillations to be completed while the tube is rising across a scale height.

### 4.3. The Asymptotic Regime of Rise

The strong initial acceleration phase is followed by a quasi-stationary asymptotic regime (Fig. 1, *lower row*). In it, the rate of change of the tube interior and external flows becomes small compared to the initial phases. The transition occurs at about  $t = 3$  (between the third and fourth panels of Fig. 1). The asymptotic regime is characterized by

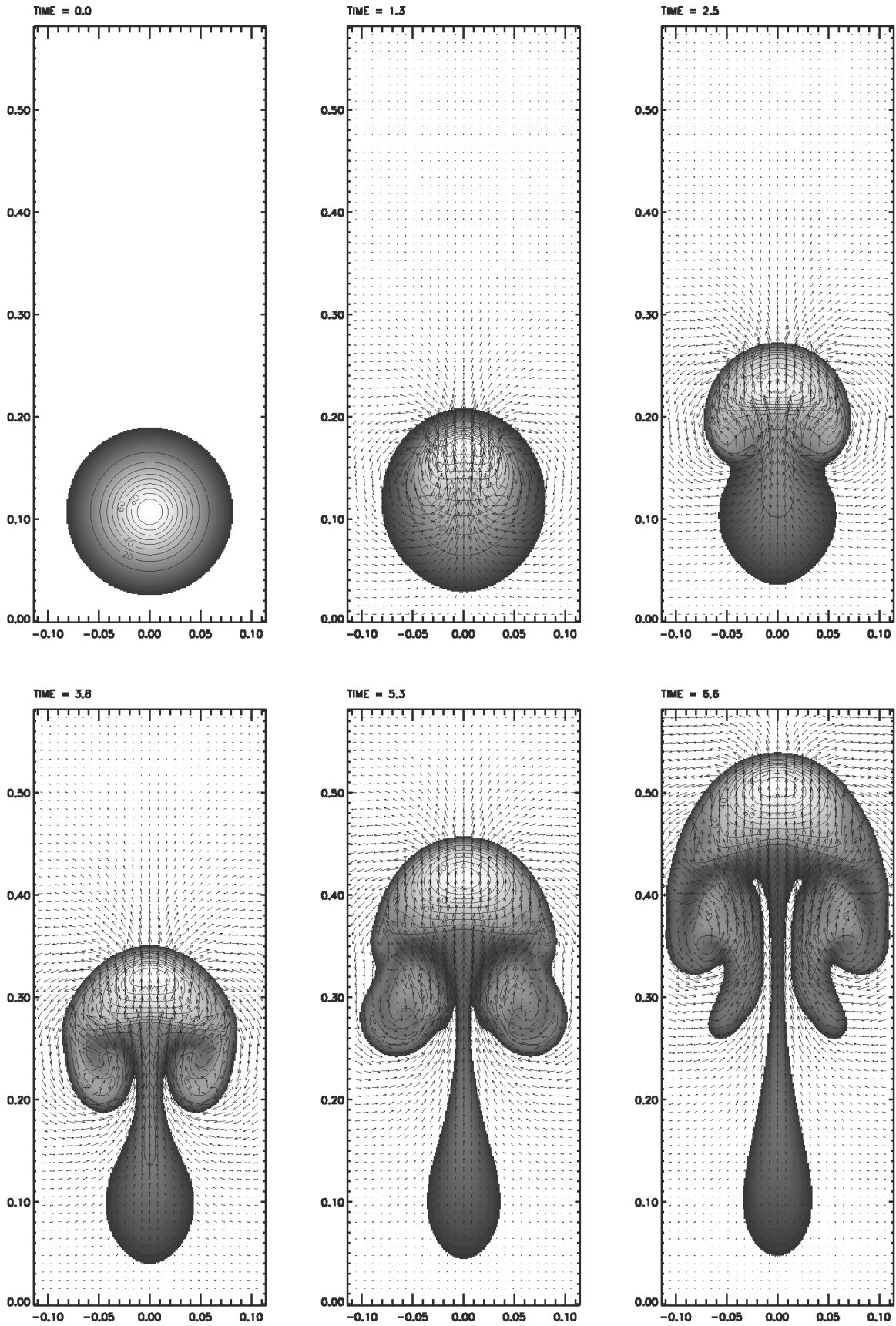


FIG. 1.—Rise of a twisted tube through a stratified environment. The initial pitch angle  $\Psi_{\text{mt}}$  is  $7^\circ$ . The gray scale and the contours correspond to the longitudinal magnetic field intensity. At each time step, white corresponds to the maximum of  $B_z$  at this instant and black to 1% of this maximum. The arrows represent the velocity field. In the figure, only a about  $1/5$  of the total integration box is reproduced; more precisely,  $100 \times 500$  out of a total of  $300 \times 700$  points for each half of the figure are included. The times represented are  $t = 0, 1.3, 2.5, 3.8, 5.3,$  and  $6.6$ . The complicated shape of the wake in the two last panels is due to the episodic release of small secondary rolls from the lateral edges of the tube (see § 6.2.3).

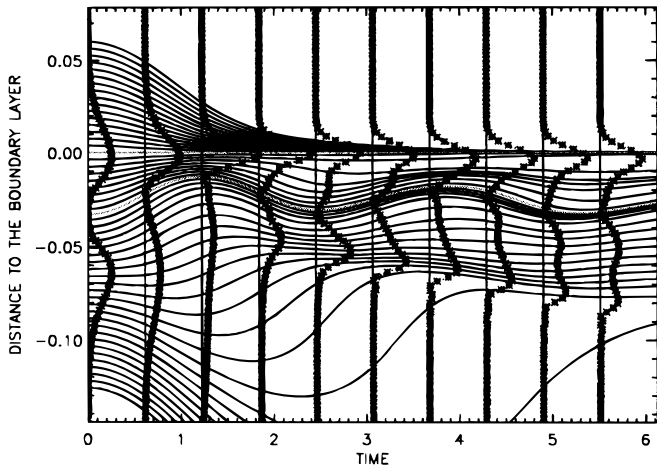


FIG. 2.—Distance to the stagnation point at the tube front of 50 mass elements initially located at equidistant points along the vertical symmetry axis, represented as a function of time (solid lines). The compression of the tube front and the oscillations of the central regions along the vertical axis can be clearly seen. The curves plotted vertically (stars) are profiles of the transverse field intensity,  $B_t$ , along the vertical symmetry axis at regular intervals of time.

the adoption of a terminal speed of rise, a sharp separation of the tube interior from its surroundings, and a well-developed trailing wake. Simultaneously, the tube stops losing magnetic flux to the wake, and there is no further important deformation of the magnetic field lines in the head of the tube. The following subsections deal with some of the features characterizing this asymptotic regime.

4.3.1. The Terminal Velocity

Once the wake is developed, the resistance of the surroundings to the advance of the tube can be calculated using the customary aerodynamic drag force with the almost constant drag coefficient  $C_D$ . In the asymptotic regime, the total buoyancy of the tube is a slowly varying

quantity. Thus, we can expect the tube to reach a terminal speed of rise given by

$$v_{\text{term}} = \left( \frac{2gS\overline{\Delta\rho}}{C_D d\rho_e} \right)^{1/2}, \tag{19}$$

where  $S$  and  $d$  are the cross-sectional area and horizontal diameter, respectively. The order of magnitude of this speed has been estimated in equation (10). The best fit to the numerical results yields a value for  $C_D$  of approximately 1.6. It is not obvious how to formulate analytically the approach to this asymptotic regime, since the coefficient  $C_D$  is not constant while the tube is changing its shape and developing a wake. The initial acceleration of the tube as a whole is

$$a = \frac{g\overline{\Delta\rho}}{i\overline{\rho}}; \tag{20}$$

the factor  $i$  allows for added inertia arising from the coacceleration of the external medium ( $i = 2$  for a rigid straight cylinder). To approximate the velocity of the tube in the initial and intermediate time-dependent phases, we use an expression for a tube starting from rest with acceleration  $a$  being acted upon by a constant driving force with a fixed  $C_D$ , i.e.,

$$v_{\text{rise}} = v_{\text{term}} \tanh\left(\frac{at}{v_{\text{term}}}\right), \tag{21}$$

where  $v_{\text{term}}$  is still given by equation (19).

The numerical results show a surprising closeness to equation (21). In Figure 4, we show with a dotted line the velocity given by equation (21), while the actual speed of the tube apex,  $v_{\text{apex}}$ , is indicated by circles. As can be seen, the tube speed oscillates around the mean speed given by equation (21). This effect is due to the strong oscillations of the tube interior; in fact, the tube center oscillates with a much larger amplitude, as is shown by the curve with aster-

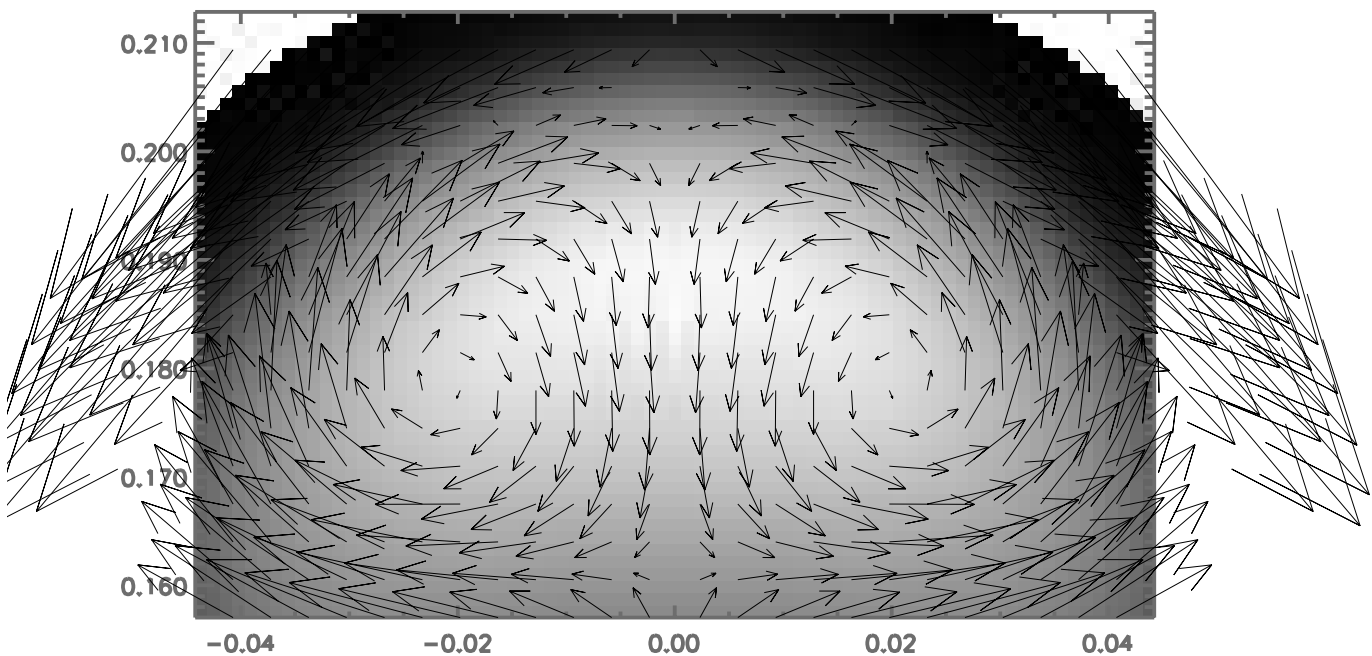


FIG. 3.—Close-up view of the tube interior showing the velocity vectors of the internal torsional oscillation at time  $t = 1.57$ . The arrows in the figure represent the relative velocity of the individual mass elements with respect to the tube apex.

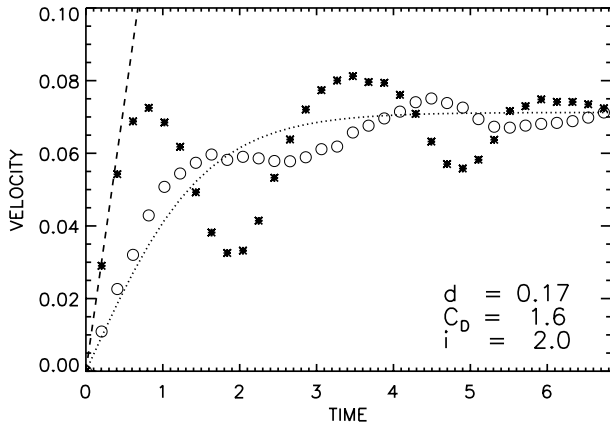


FIG. 4.—Velocity of the tube center (stars) and of the apex (circles) as a function of time. The dotted line corresponds to eq. (21). The dashed line represents the initial acceleration of the tube center,  $(|\Delta\rho/\rho|)_{r=0}g/i$ , with  $i = 2$ .

isks. The tube center *pushes* the apex, so that the circles and asterisks are slightly out of phase. The amplitude of the oscillation diminishes as its energy is radiated to the external medium and both curves converge toward the dotted line. The initial acceleration of the tube apex is very close to equation (20) with  $i = 2$ , i.e., it corresponds to the global buoyancy of the tube. The tube center, in turn, has a higher acceleration, corresponding to the local value of the buoyancy, namely  $(|\Delta\rho/\rho|)_{r=0}g/i$  (this value is shown in the figure as a dashed line). Here again, the enhanced inertia factor  $i$  must be set to equal 2.

As a test of the validity of the terminal velocity formula, we have calculated the evolution of tubes starting with the same initial condition as that used for Figure 4 (in particular, the same tube radius,  $R$ ), but with  $\beta_0$  chosen in a range between 1000 and 100. The velocity curves of all these tubes are similar to those shown in Figure 4, with the timescale contracted by a factor  $\beta_0^{1/2}$  and the velocity scale enlarged

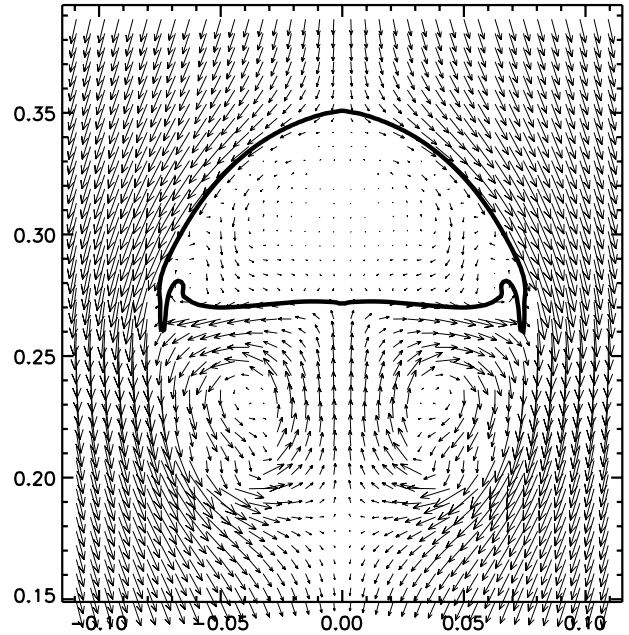


FIG. 5.—Equipartition line at  $t = 3.8$ , together with the flow field relative to the apex of the tube. The simple structure of the wake at this time is clearly visible. The envelope of the tube and the wake has a well-defined elliptical shape. This figure bears a strong resemblance to the experimental results of air bubbles rising in liquids (e.g., Collins 1965; also reproduced by Batchelor 1967, Plate 15).

by the same factor. More precisely, if all these tubes reach the aerodynamic drag regime with the terminal velocity given by equation (19), then the curves depicting the velocity of the apex normalized by the plasma  $\beta$ ,  $v_{\text{apex}}\beta_0^{1/2}$ , versus the position of the apex must all basically coincide (the drag coefficient  $C_D$  does not change much with varying Reynolds number in this regime). The results of the tests indeed show a large degree of superposition of those curves; the maximum relative deviation between them is a factor of 1.1,

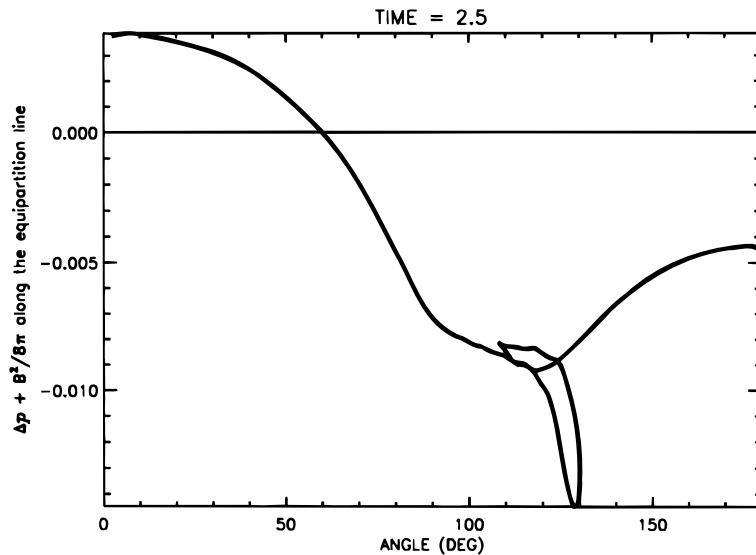
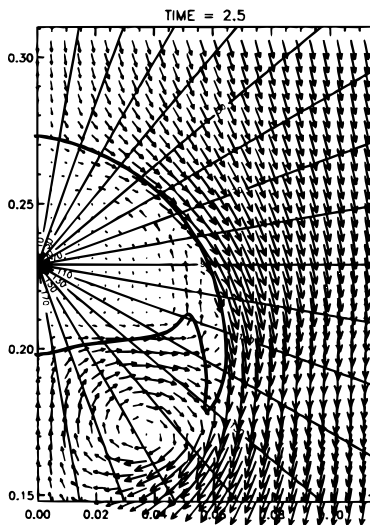


FIG. 6.—Profile of the total pressure excess along the boundary of the tube, defined by the equipartition line (see § 4.3.2) at time  $t = 2.5$ . The boundary of the tube (the equipartition line) is shown as a thick line in the left panel. The feature in the middle of the profile (between  $110^\circ$  and  $130^\circ$ ) results from the shape of the equipartition line at the lateral edge of the tube. The arrows in the left panel correspond to  $v_{\text{ret}}$ , and the radial lines are drawn at constant azimuthal angles.

which can be attributed to the change in  $C_D$  consequent to the variation in the Reynolds number.

#### 4.3.2. The Equipartition Line at the Tube Periphery

As a result of the resistance to deformation provided by the transverse field, there is a neat separation between the tube interior and exterior in the asymptotic regime. A good indicator of the location of the tube boundary can be obtained by comparing the kinetic energy density of the relative flow field,  $v_{\text{rel}} \equiv v - v_{\text{apex}}$ , i.e.,  $e_{\text{kin}} \equiv \rho v_{\text{rel}}^2/2$ , with the energy density of the transverse magnetic field,  $e_{\text{magr}} \equiv B_t^2/(8\pi)$ . We define the *equipartition line* as the locus of those points in the tube periphery where the two energy densities are equal. Figure 5 shows, at time  $t = 3.8$ , the relative flow field  $v_{\text{rel}}$  and, superposed on it, the equipartition line. The flow field changes markedly when crossing the equipartition line; the velocities inside are much smaller than those outside. In other words, once the terminal velocity has been reached, the tube rises basically as a unity, with only a weak internal flow pattern, corresponding mainly to the torsional oscillations described in the previous section. A comparison of Figure 5 with the results of laboratory experiments (e.g., Collins 1965; Plate 15 in Batchelor 1967) shows that there are striking similarities between buoyant magnetic tubes and air bubbles rising in a liquid, both in the shape of the rising object itself as in the wake, in spite of the very different parameter values involved (such as, e.g., the density deficit).

All along the initial phase, a pressure profile is set up around the tube periphery that closely resembles the pressure distribution around rigid cylinders in relative motion to their surroundings. To show this, we can plot (see Fig. 6) the pressure in the points along the equipartition line. In this figure, the pressure excess associated with the return flow between the vortex rolls of the wake is clearly visible.

#### 5. THE SHARP INTERFACE AT THE TUBE BOUNDARY: MAGNETIC BOUNDARY LAYER

All around the equipartition line there is a region with nonzero vorticity. This contains (1) a boundary layer surrounding the tube and (2) the trailing wake. Farther out, there is the external medium, with a largely vorticity-free flow. In this section, we study the structure of the boundary layer; the wake is considered in § 6.

The two main physical features that characterize the magnetic boundary layer around the tube are a strong shear of the tangential flow and high magnetic field gradients. These lead to enhanced generation of vorticity, ohmic diffusion, and the generation of entropy. In the following subsections we study these items in turn.

##### 5.1. Shear Flow and Field Gradients

A pronounced shear is taking place in a thin band around the equipartition line (Fig. 5). As a result, the matter elements and the transverse field are being stretched at the tube periphery all around the tube. To visualize this phenomenon, we use *Lagrange markers* that follow the motion of the tube's mass elements (Fig. 7). We choose six groups of markers at time  $t = 0$  (*left panel*) at a distances of the tube center such that  $B_t$  is 5% (*white asterisks*), 27% (*triangles*), and 77% (*diamonds*), respectively, of  $B_{t0}$  (the maximum value of  $B_t$  in the tube) in both the upper and lower half of the tube. The markers are set in the neighborhood of the tube axis and are left to evolve with the tube. As time advances, the markers of the outermost group in the upper tube half are stretched by a very large factor along the tube periphery (Fig. 7, *center and right panels*); in fact, many of them are brought all the way down to the wake. The markers of the group immediately below them (*triangles*) are brought close to the uppermost group and stretched,

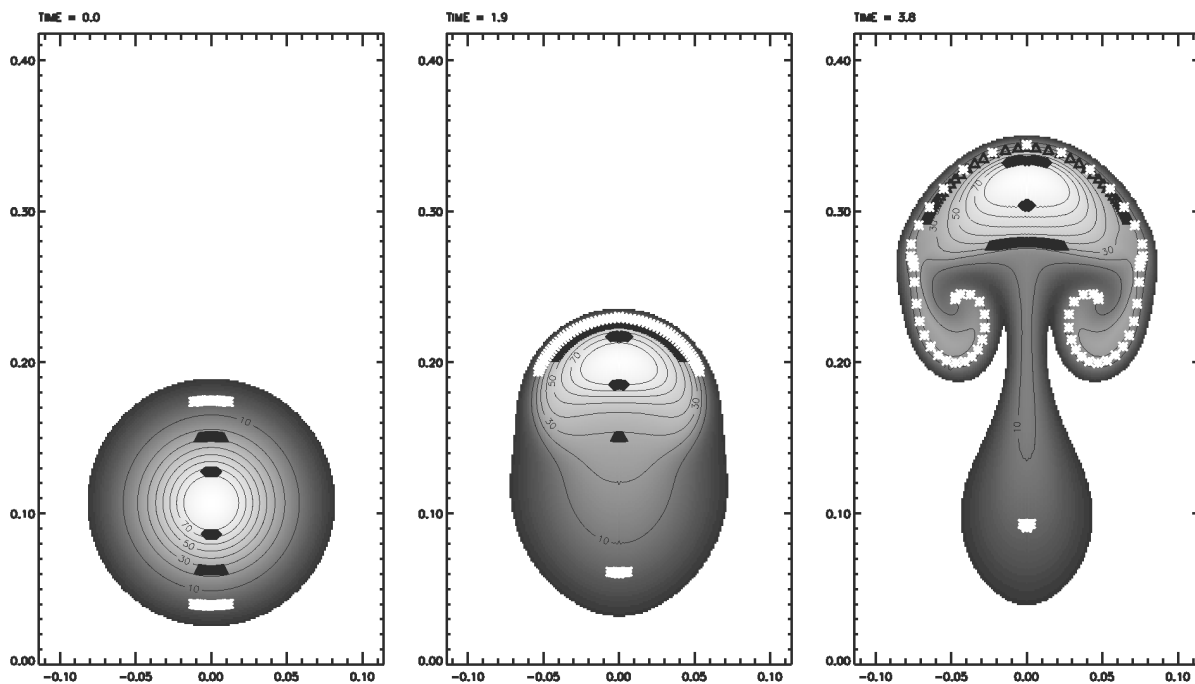


FIG. 7.—Motion of individual mass elements in the tube, showing the stretching of the matter and field along the tube boundary. The panels correspond to  $t = 0, 1.9,$  and  $3.8$ . At time zero, the Lagrange markers are located at  $R/H_p = 0.024, 0.044,$  and  $0.068$ , where  $B_t$  is equal to 77%, 27%, and 5% of its value at the center. Radial compression, azimuthal stretching, and shearing of the upper layers of the tube are apparent. The elements indicated by black triangles at the back are also somewhat stretched as a result of flow in the wake.

albeit by a smaller factor than the other group. Large compression and stretching occur basically only in the neighborhood of the interface between the tube and its surroundings; closer to the tube center (*diamonds*), the mass elements are only periodically moved following the internal torsional oscillation. At the rear of the tube, the Lagrange markers with  $B_t = 0.27B_{t0}$  (*triangles*) are also somewhat stretched by the flow of the trailing wake (see § 6). The outermost parcels at the back of the tube (*white asterisks*) are trapped in the tail and no longer rise with the tube.

Corresponding to this shearing, the pitch angle increases to large values at the tube periphery; in Figure 8 we plot the pitch angle distribution along the vertical axis of symmetry for the three instants shown in Figure 7. The pitch angle becomes large in the interface at the tube front (*middle panel*). In the quasi-stationary regime, its distribution shows a horizontal asymptote outside the tube similar to that of the initial condition. This feature is *not* merely a consequence of our initial condition given in equation (8). In fact, an initial pitch angle distribution with exponential decline for large radius at time  $t = 0$  (see eq. [9]) yields in the quasi-stationary regime a horizontal asymptote similar to that of Figure 8. It is then perhaps more natural to choose the initial condition of equation (8) from the outset.

The large pitch angles apparent at the right of Figure 8 are all in a region of the tube where the magnetic field intensity is very low; the central regions, on the other hand, have low pitch angles. Thus, one should not expect a global kink-unstable behavior of the tube. This can be checked by calculating the net tension in the tube over background (see § 9.2 in Parker 1979). With the convention that tension is positive and pressure negative, we obtain a positive value indicating that the tube is under longitudinal tension rather than compression. Thus, there should be no tendency to buckling of the tube.

### 5.2. Vorticity Generation in the Boundary Layer

The large jump in tangential speed visible across the equipartition line in Figure 5 marks the presence of a *vortex sheet* surrounding the tube. In fact, vorticity (more precisely, its longitudinal component  $\omega_l$ ) is generated at the boundary layer during the whole duration of the run. From there, it is advected toward the wake.

These processes are governed by equation (14). As in § 3.1, the right-hand side of this equation is dominated by the first two terms [the third is again  $O(1/\beta_0)$  smaller]. However, along the front of the tube, those two terms, i.e., the gravitational and magnetic vorticity sources, *reinforce each other* rather than mutually cancel, as in the tube interior. This is because the radial derivative of the transverse field component reverses its sign in the neighborhood of the equipartition line. For instance, in the simple case in which the field lines are still not far from circular (e.g., along the front) the magnetic contribution is approximately

$$\frac{\nabla \times \mathbf{F}_{Lt}}{\rho} \simeq \frac{B_t}{c\rho} \frac{\partial}{\partial \phi} \left[ \frac{1}{r} \frac{\partial}{\partial r} (rB_t) \right] \simeq \frac{B_t}{c\rho} \frac{\partial}{\partial \phi} J_t, \quad (22)$$

so that  $J_t$  changes sign at about the maximum of  $B_t$ . As a result, (and taking into account the sign of the azimuthal derivative  $\partial/\partial\phi$ ), in the right half of the tube, positive vorticity is generated all along the front of the tube, and negative vorticity is generated at the rear, i.e., at the interface between the tube and the wake. At the rear,  $\nabla(\Delta\rho/\rho)$  is

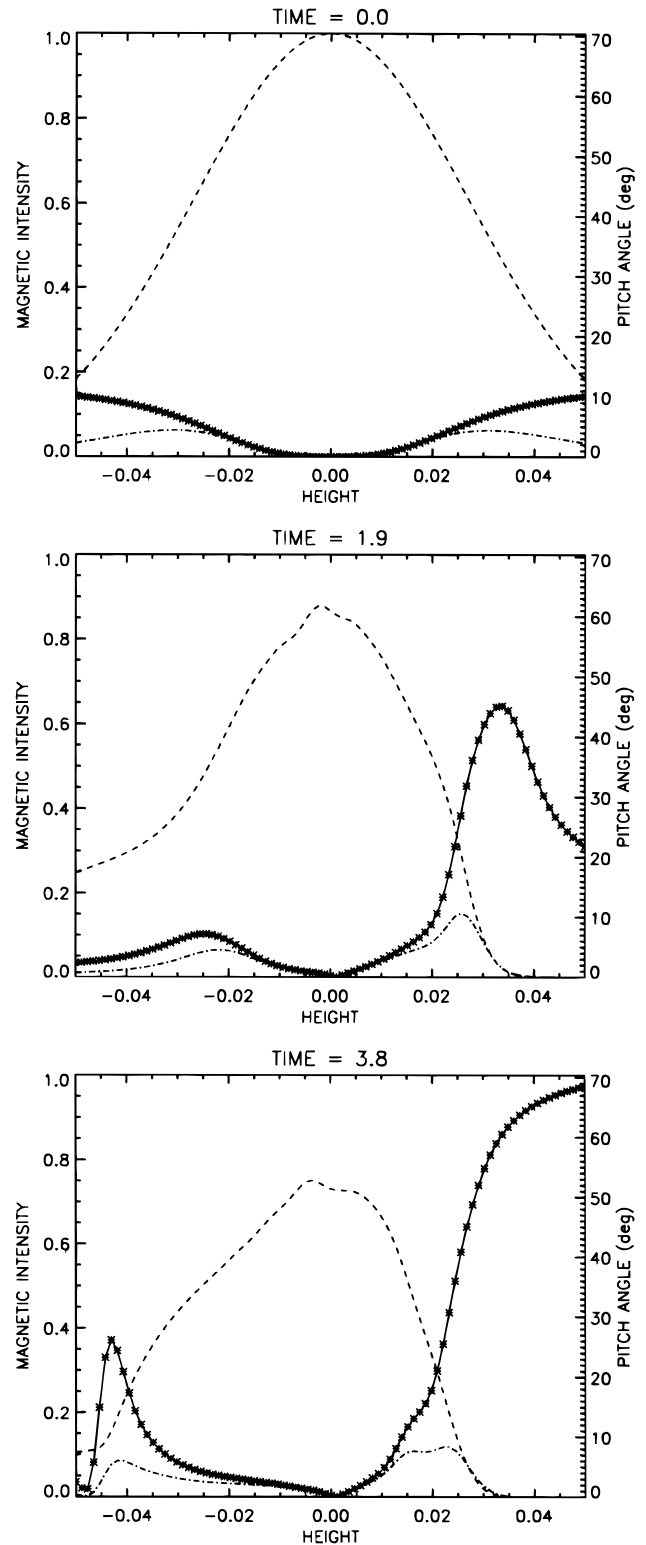


FIG. 8.—Pitch angle distribution (*stars*) along the vertical central axis at three different times corresponding to the three panels of Fig. 7. The profiles of  $B_t$  (*dashed line*) and  $B_l$  (*dot-dashed line*) are overplotted.

approximately parallel to  $\mathbf{g}$ , and therefore the magnetic stress is at any rate the main source of vorticity there.

In Figure 9, we show the distribution of vorticity in the box at four different times during the evolution. White and black indicate positive and negative vorticity, respectively (i.e., clockwise and anticlockwise rotation), while the gray

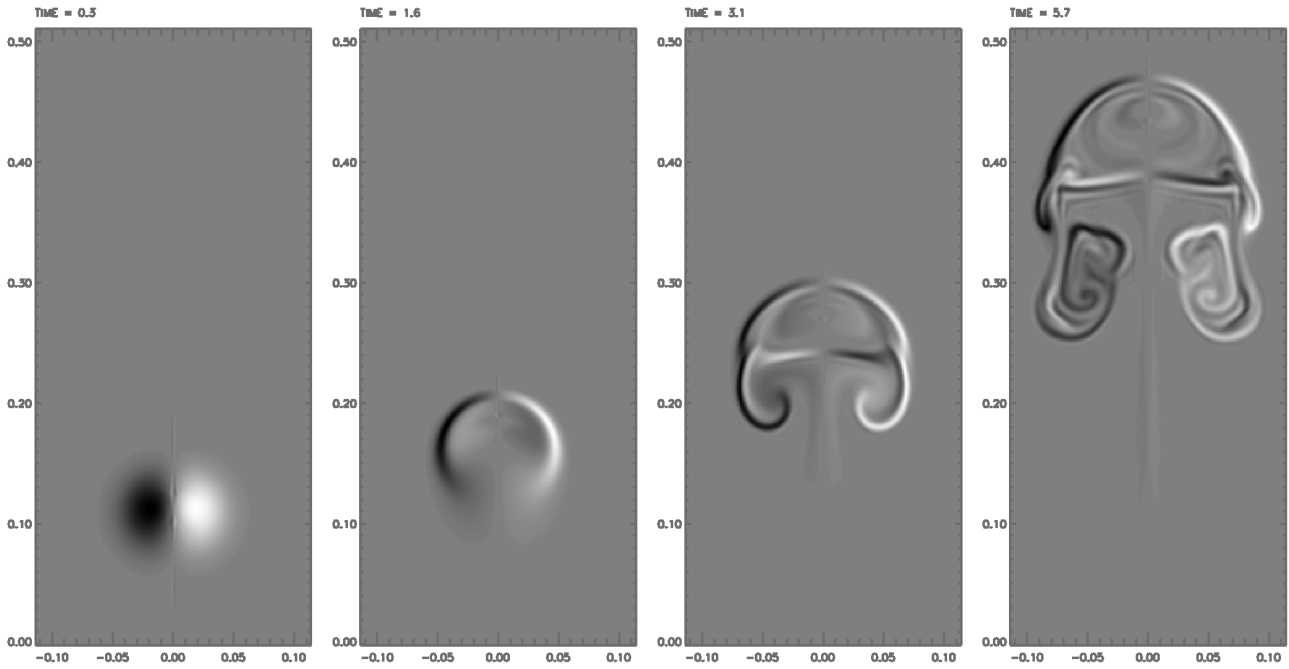


FIG. 9.—Distribution of the  $y$ -component of the vorticity vector in and around the tube at  $t = 0.3, 1.6, 3.1,$  and  $5.7$ . White corresponds to positive vorticity (clockwise rotation) and black to negative. The two leftmost panels clearly show the vorticity associated with the torsional oscillations. The boundary layer and vortex sheet at the tube front are visible in the three rightmost panels. In the two last panels, the vortex sheet at the interface between the wake and the tube is also visible.

background is the zero vorticity level. Soon after the beginning (*leftmost panel*,  $t = 0.3$ ) the gravitational torque is creating positive and negative vorticity in the right and left tube halves, respectively, across the whole tube interior. In the second panel ( $t = 1.6$ ), this has already been countered by the magnetic tension of the transverse field; the reversal of the sign of the vorticity in the interior reveals the first backward torsional oscillation. In addition, a vortex sheet is already apparent all around the tube front. At the rear, there is only an incipient wake and no clear vortex sheet yet.

The third and fourth panels correspond to the asymptotic phase ( $t = 3.8$ , i.e., close to the beginning of the stationary regime, and at an advanced stage,  $t = 5$ , respectively). Vorticity generation now occurs basically close to the equipartition line only. Vortex sheets along *both* the front and the rear of the head of the tube are visible. As expected, the signs of their vorticity are opposite. A detailed distribution of  $\omega_l$  in the boundary layer around the tube (from top to bottom), can be seen in Figure 10. The vorticity indeed changes sign at the edge of the tube; the abrupt shape of the

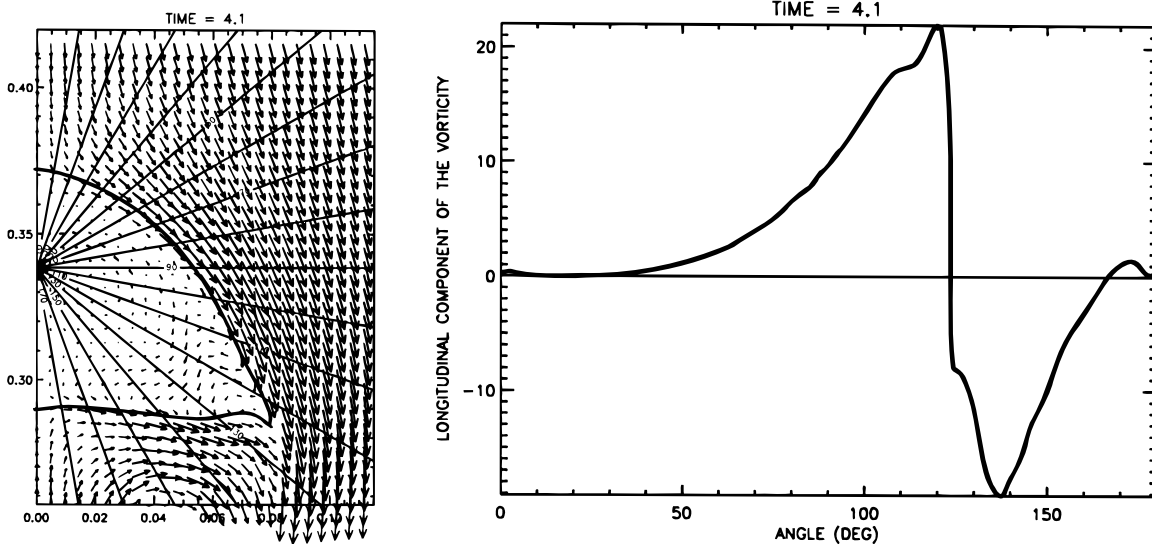


FIG. 10.—Profile of the longitudinal component of the vorticity (*right panel*) along the equipartition line drawn in the left panel for  $t = 3.8$ . The zero-crossing at about  $120^\circ$  corresponds to the transition from tube front to rear at the edge of the tube. The radial lines in the left panel are drawn at constant azimuthal angles.

zero crossing is due to the acute shape of the latter. The small maximum at the right end of the distribution is characteristic of the tail (§ 6.2).

5.3. Ohmic Diffusion and Field Advection

The structure of the magnetic boundary layer is dominated by ohmic diffusivity, which in part, in the present case, takes on the role played by viscosity in the standard hydrodynamic boundary layers. An important difference between viscous and purely magnetic boundary layers, however, lies in the no-slip condition for the flow; in the purely magnetic case, there is no counterpart to the viscous second-order derivative term that could force the tangential velocity to reach a zero value at the boundary. In our case, however, the flows on the inner side of the equipartition line are reduced or suppressed by the magnetic forces. In other words, in the present boundary layer, the Lorentz force imposes a *no-slip* condition that does not allow either penetration of the external incoming flow into the tube or large fluctuations of the transverse velocity inside. This is clearly visible in Figure 11, where we have plotted  $v_x$ ,  $(v_{rel})_z$ ,  $B_t$ , and  $B_l$  along a vertical axis slightly offset from the symmetry axis.

The slope of the profile of  $B_t$  and  $B_l$  across the boundary layer results from the equilibrium between the outward ohmic diffusion and the field advection through the external flow. For  $B_t$ , for instance, this is controlled by the transverse component of the induction equation (eq. [3]). Written in terms of the magnetic potential  $A$ , this reads:

$$(v_{rel} \cdot \nabla)A = \eta \Delta A, \quad \text{with } B_t \equiv \nabla \times (A i_y). \quad (23)$$

As the transverse field diffuses outward, it *swallows* some of the incoming external matter (which, in this way, slowly enters the magnetic field system). Simultaneously, this same external matter *advects* the magnetic field back toward the tube interior. The equilibrium between those two terms is reached for a given thickness of the boundary layer,  $L_{bl}$ . To obtain an estimate for  $L_{bl}$ , we note that the external flow has a length scale comparable to the tube radius (a common

feature of cylinders moving in fluid media), so that

$$L_{bl} \sim \frac{R}{Re_m^{1/2}}. \quad (24)$$

This estimate is in agreement to within a factor of about 2 with the results of the numerical calculation (see Fig. 11). An analogous advection-diffusion equilibrium can be seen to hold for  $B_l$  in the boundary layer.

5.4. Comparison with Air Bubbles and Rigid Tubes

In spite of the striking similarities between the present problem and the rise of an air bubble, the corresponding boundary layers at the periphery of the rising object differ in important ways. The boundary of an air bubble is basically a *free surface* for the external medium, since the density and viscosity in the interior are negligible compared to those outside. The external flow must then satisfy a zero tangential stress boundary condition rather than the no-slip condition of the present magnetic tube (e.g., Batchelor 1967, § 5.14; Ryskin & Leal 1984a, 1984b). As a consequence, the tangential velocity at the gas/liquid interface in the air bubble does not vanish, but must instead satisfy the following equation:

$$\omega_l = 2\kappa(v_{rel})_{tg}, \quad (25)$$

with  $\kappa$  being the curvature of the boundary layer and  $(v_{rel})_{tg}$  the tangential component of the relative flow speed. The resulting jump in tangential velocity across the boundary layer of a bubble is therefore only on the order of  $Re^{-1/2}$ , while it is  $O(1)$  for a no-slip boundary layer, as in the present problem.

The magnetized boundary layer of the rising tube, in fact, more closely resembles the boundary layers around solid bodies with a no-slip condition than those around air bubbles. The distribution of vorticity along the equipartition line shown in Figure 10 is quite similar to that around the boundary of a rigid cylinder at  $Re \simeq 300$  (e.g., Ta Phuoc Loc 1980). In our case, however, the reversal of the sign occurs more abruptly because of the particular geometry of the equipartition line.

5.5. Entropy Generation

The enhanced ohmic dissipation in the boundary layer is creating entropy at a rate given by

$$\frac{D}{Dt} \left( \frac{\Delta s}{c_p} \right) = \eta \frac{\gamma - 1}{\gamma} \frac{(\nabla \times \mathbf{B})^2}{4\pi p}. \quad (26)$$

To order of magnitude, this entropy increase can be written as

$$\frac{D}{Dt} \left( \frac{\Delta s}{c_p} \right) \approx \frac{1}{\beta_{bl}} \frac{v_{rise}}{R}, \quad (27)$$

with  $\beta_{bl}$  being the local plasma  $\beta$  in the boundary layer. The entropy increase for a matter element moving all along the tube boundary is then of order  $1/\beta_{bl}$ . As a result, the density difference  $\Delta\rho/\rho$  of those elements can be substantially modified. This, however, is unlikely to cause important modifications in the dynamical behavior of the tube boundary. The main driving force there, the pressure gradient, is on the order of  $\rho v_{rise}^2/R$ ; therefore, it should be more important than the local gravitational term  $g\Delta\rho$  by the ratio  $B_0^2/B_{bl}^2 \gg 1$ , where  $B_{bl}$  is the magnetic field strength in the boundary layer.

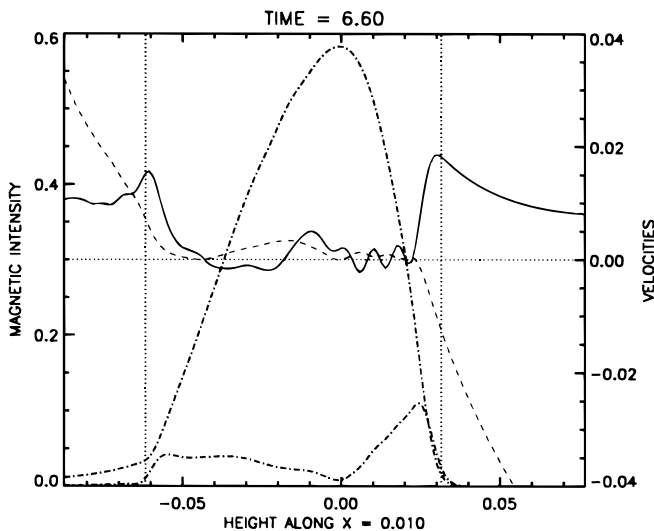


FIG. 11.—Plots of  $B_t$  and  $B_l$  (dash-dotted line) together with  $v_x$  (solid line) and  $(v_{rel})_z$  (dashed line) along a vertical axis at  $x = 0.01$  at time  $t = 6.60$ . The vertical dotted lines correspond to the positions where  $e_{mag} = e_{kin}$ .

In our numerical simulation, we also find some increase of entropy because of the artificial viscosity. Its influence, however is only secondary, because of the low value of  $Re_m$  chosen.

## 6. THE WAKE

Wakes have been the object of active research in fluid dynamics for at least the past four decades. This includes the wake behind solid cylinders (e.g., Collins & Dennis 1973a, 1973b; Ta Phuoc Loc 1980; Bouard & Coutanceau 1980; Ta Phuoc Loc & Bouard 1985), drops (Dandy & Leal 1989; Stone 1994), and air bubbles (Davies & Taylor 1950; Collins 1965; Parlange 1969; Wegener & Parlange 1973; Hnat & Buckmaster 1976; Ryskin & Leal 1984b; Christov & Volkov 1985). In this chapter, we briefly describe the formation and structure of the wake behind the rising magnetic tube and pay special attention to the similarities and differences with other wakes known in the literature.

### 6.1. The Time Evolution of the Wake

Solid cylinders, air bubbles, and drops all have a clearly defined boundary from the beginning. Vorticity is created along the boundary and advected downflow. The wake is formed out of external fluid only, via, e.g., in solid bodies, the detachment of the boundary layer. In our case, in contrast, there is no such clear boundary at the beginning. The layers of weak magnetic field in the outskirts of the tube (1) are unable to resist the incipient external flow, so that they are bodily convected to the rear, and (2) increase their vorticity through the mechanisms explained in § 3.1.2 and § 5.2. It is the accumulation of this rotating material at the back of the tube that constitutes the wake. The material making up the wake may in fact be a large fraction of the initial tube in the case of small initial pitch angles (see § 7).

The formation process of the wake is basically complete by  $t = 3.0$  (see Figs. 1 and 5), and this signals transition to the asymptotic regime of rise (see § 4.3). The latter, however, is not exactly stationary, since the wake does not remain unmodified in the rest of the evolution. In fact, it slowly grows in size and episodically changes its shape. This growth can be seen in Figure 12, where the vertical size of the rolls is depicted as a function of time. The elongation is

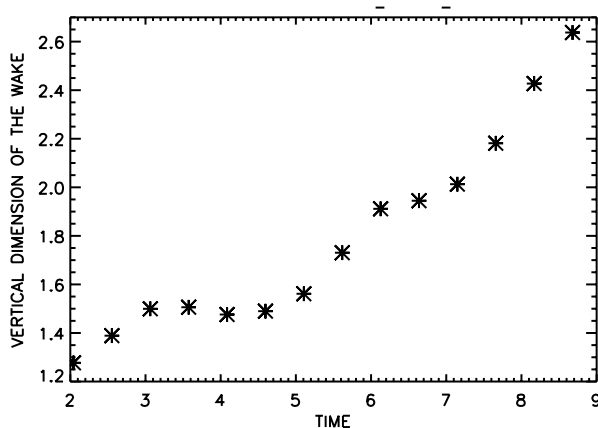


FIG. 12.—Vertical size of the wake as a function of time, calculated as the distance between the stagnation point at the rear of the tube and the stagnation point at the bottom of the wake. The growth is quasi-linear, with oscillations superposed.

roughly linear, with a small-amplitude oscillation superimposed. This kind of behavior is not unknown in fluid dynamics. The elongation of the wake is indeed similar to what is observed behind a rigid cylinder moving at constant speed, with  $Re \approx 300$ , after an impulsive start (see Ta Phuoc Loc 1980); in the laboratory experiment, the linear growth of the wake with time continues well after the high- $Re$  flows have been set up around the cylinder and  $C_D$  has reached a constant value close to 1. For higher values of  $Re$  ( $= 3000$ ), the growth of the wake with time is exponential rather than linear (Ta Phuoc Loc & Bouard 1985). In our case, a small part of the growth of the wake is due to stratification, but its main cause is the transport of rotating material from the boundary layer along the boundary of the tube to the wake. This is clearly visible in the third and fourth panels of Figure 9: a white *streamer* of positive vorticity coming from the tube front is being wrapped up first around and then into the roll on the right-hand side of the wake. Simultaneously, a black *tongue* with its origin at the back of the tube is also making inroads into the wake, next to and following a path parallel to the white streamer.

In the case of rigid tubes and bubbles moving through a fluid (and assuming perfect symmetry about the object's midplane), the growth of the wake normally lasts until a dynamical equilibrium is adopted. In this, the vorticity generated in the boundary layer is advected to the wake, where it is redistributed through viscous diffusion and further advection. Simultaneously, the energy gained through the driving force (the potential energy for the bubbles) is transformed into heat in the wake, again through viscous dissipation (Parlange 1969; Wegener & Parlange 1973). Further changes may occur if there is no mechanism to dispose of the heat so generated.

In the results presented here, no dynamical equilibrium is reached, since there is no equivalent mechanism to diffuse the vorticity effectively. This can be seen quantitatively from the fact that the characteristic time for the adoption of a stationary state in the wake through viscous diffusion and dissipation is  $Re (L_{\text{wake}}/R)^2$  times longer than the characteristic time for the formation of the wake itself,  $L_{\text{wake}}$  being the transverse dimension of the wake and  $Re$  the viscous Reynolds number. In our case,  $L_{\text{wake}} \approx R$ , and we expect  $Re$  (calculated on the basis of the numerical viscosity) to be at least as high as  $Re_m$ . Therefore, the establishment of dynamical equilibrium lasts much longer than the evolution presented in this paper. The consequence of this is the very inhomogeneous vorticity distribution apparent in Figure 9. A high- $Re$  case, in fact, may never come to full dynamical equilibrium, because an instability interrupts the approach to a steady state; the two standing rolls develop asymmetric oscillations until one of them is released downstream (see, e.g., Batchelor 1967, Plate 10). In contrast, in low- $Re$  bubble experiments, the trailing vortex rolls are similar to a Hill's vortex (e.g., Collins 1965; Parlange 1969; Wegener & Parlange 1973; Ryskin & Leal 1984b; Christov & Volkov 1985).

### 6.2. Further Structural Features in Common with Laboratory Experiments

#### 6.2.1. The Skirt

In experiments with buoyant air bubbles, it is often observed that a small quantity of air is torn off (or sucked from) the bubble corner and becomes stretched all around

the wake. The result, commonly called the *skirt*, is a sheet of air aligned with the interface between the wake and the external medium that remains attached to the bubble (e.g., Hnat & Buckmaster 1976). A similar feature can be identified in our numerical simulations, coinciding with the streamers or tongues of vorticity of both signs mentioned in the last section. In contrast to the air bubbles, the *skirt* here is made of magnetized material. During the whole rise, the magnetic field in the skirt is continuously compressed and stressed by both the wake and the external flows.

### 6.2.2. The Tail

All along the central symmetry plane, the rising tube leaves behind a *tail* of weakly magnetized matter (Fig. 1). Its upper part is compressed by the two rolls of the wake. In fact, the *tail* is not only magnetized, but also has nonzero vorticity. This can be seen both in the distribution of Figure 10 (maximum of positive vorticity at the right end of the figure) and as a light shadow in the vorticity map of Figure 9. Similar structures are seen behind moving pairs of vortices, as well as in bubble experiments (e.g., Wegener & Parlange 1973). The total amount of magnetic flux lost by the tube to the tail is small (only 6% of the total flux).

### 6.2.3. The Secondary Rolls at the Edge of the Tube

Close to the lateral edges of the tube (see Fig. 13 and the last panel in Fig. 9), small secondary rolls are built from time to time; they grow for a while and then are released to the downflow. These features are reminiscent of the secondary rolls observed near the detachment point of the boundary layer around solid cylinders (Ta Phuoc Loc 1980; Ta Phuoc Loc & Bouard 1985). These secondary rolls strongly perturb the skirt and the wake when they are released; this is the main cause of the irregular shape of the wake in the last panels of Figures 1 and 9.

## 7. THE RISE OF TUBES WITH DIFFERENT INITIAL DEGREES OF TWIST

The initial value of  $\Psi_{mt}$  for the tube with the rise we have

described in the foregoing sections was close to the value given by the criterion of equation (11), namely,  $\Psi_{mt} = 6^\circ$ . This criterion provides a lower bound for the twist necessary to withstand the destruction of the tube through vorticity generation in its interior, external pressure forces, and so forth; we do not know yet how sharp that bound is. In the present section, we investigate the transition from low-twist to high-twist regimes. We conclude that the change from one to the other is gradual and takes place over a range of, say,  $5^\circ$  in  $\Psi_{mt}$ , around the value given by the right-hand side of equation (11). In Figure 14, we show the relative flow,  $v_{rel}$  (*upper panels*), and the contours of longitudinal magnetic intensity,  $B_l$  (*lower panels*), for four cases with  $\Psi_{mt} = 13.9^\circ, 7^\circ, 2.5^\circ$ , and  $0^\circ$ , respectively. There is a clear gradation of properties and evolutionary patterns along the four columns of the figure. The amount of flux remaining in the *head* of the tube is an increasing function of  $\Psi_{mt}$ . This can be seen in Figure 15; the stars, representing the percentage of the initial flux remaining in the head, go from more than 80% for  $\Psi_{mt} = 13.9^\circ$  to about 20% for  $\Psi_{mt} = 2.5^\circ$  and (trivially) 0% for  $\Psi_{mt} = 0^\circ$ . In this figure, the change between the two regimes occurs between, say,  $3^\circ$  and  $8^\circ$ .

Not only the size, but also the shape of the remaining head varies markedly from one case to the other (see Fig. 14, *upper panels*). For  $\Psi_{mt} = 13.9^\circ$ , the tube maintains its roundish shape all along. This is especially striking at the rear of the tube; the rising return flow between the two rolls in the wake cannot dent the back of the tube. This case is closest to the motion of a rigid cylinder in a fluid. For  $\Psi_{mt}$  decreasing down to  $2.6^\circ$ , the back of the tube becomes first flat and then concave through the action of the return flow. This transition coincides with the increase of the magnetic Weber number up across unity;  $We$  is 0.19, 0.74, and 5.75 for  $\Psi_{mt} = 13.9^\circ, 7^\circ$ , and  $2.5^\circ$ , respectively. In the untwisted case, there is no longer a neat separation between tube interior and external flows. The rolls in the wake now contain 70% of the original magnetic flux, with most of the rest contained in the upper arch linking them. The evolutionary pattern in this case is similar in many respects to the

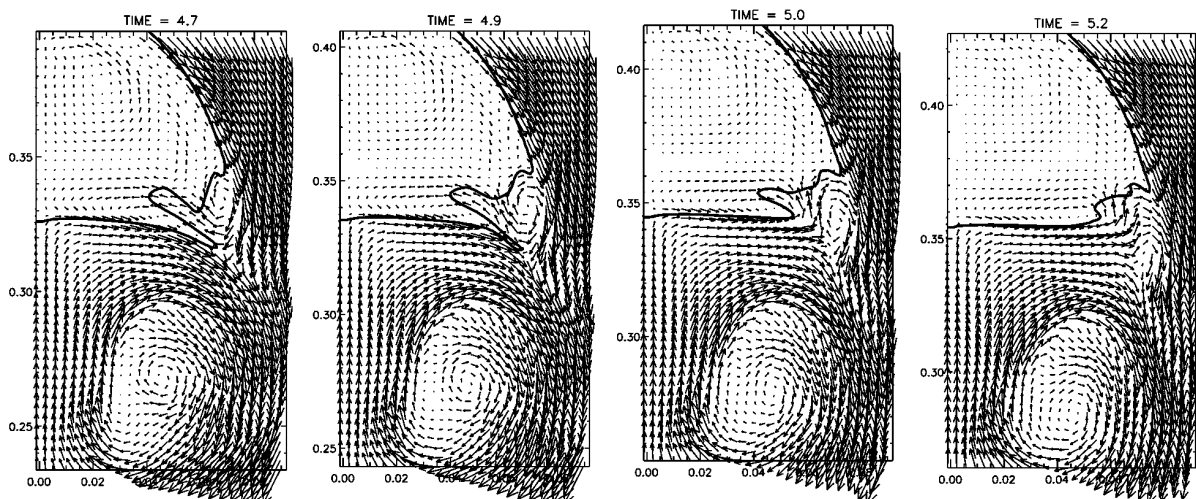


FIG. 13.—Formation and release of a secondary roll at the edge of the tube. The panels contain a time series showing the equipartition line and the relative flow field. The secondary roll is being released to the downflow; later on, it gets dragged all around the wake and noticeably perturbs the shape and velocity distribution. Note also the jumps in velocity inside the main roll of the wake, revealing the presence of vortex sheets that have been advected from the tube front.

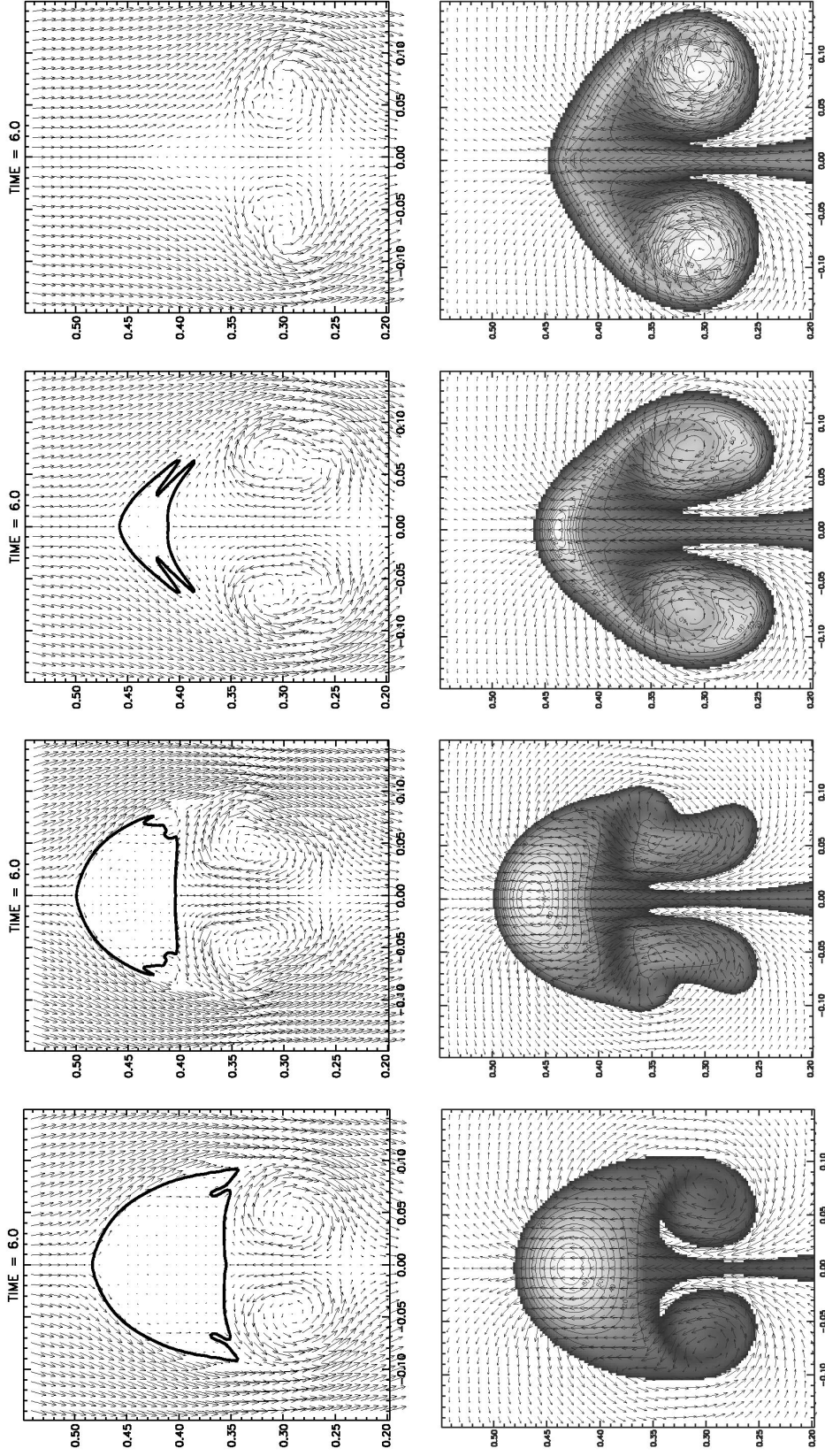


FIG. 14.—Tube and wake structure for four cases with different initial pitch angle but otherwise equal initial conditions. From left to right, the values of  $\Psi_{mt}$  were 13:9, 7° (i.e., the case studied in the rest of the paper), 2:5, and 0°. The lower panels show the general flow field and the contours of magnetic intensity for  $B_1$ . The upper panels show the velocity relative to the apex of the tube and the corresponding equipartition line (as defined in § 4.3.2). The transition from a convex tube back to a flat and then to a concave tube for decreasing initial  $\Psi_{mt}$  (i.e., as the Weber number increases) is apparent. In the untwisted case, no *head* is left, but rather there is a bridge joining the two vortex rolls of the wake.

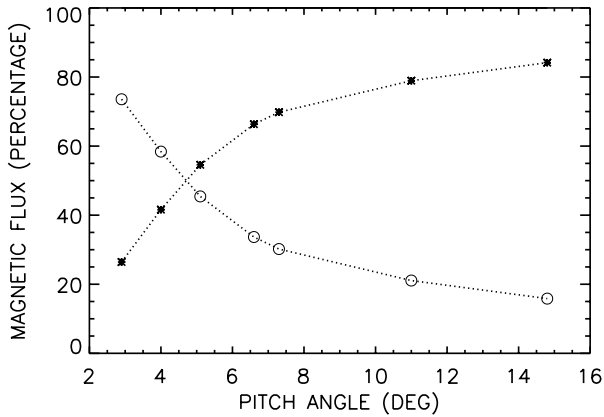


FIG. 15.—Percentage of the initial magnetic flux remaining in the head of the tube once the terminal velocity has been reached (stars) as a function of  $\Psi_{mt}$ . Also shown is the percentage of flux that has been dragged to the wake (circles).

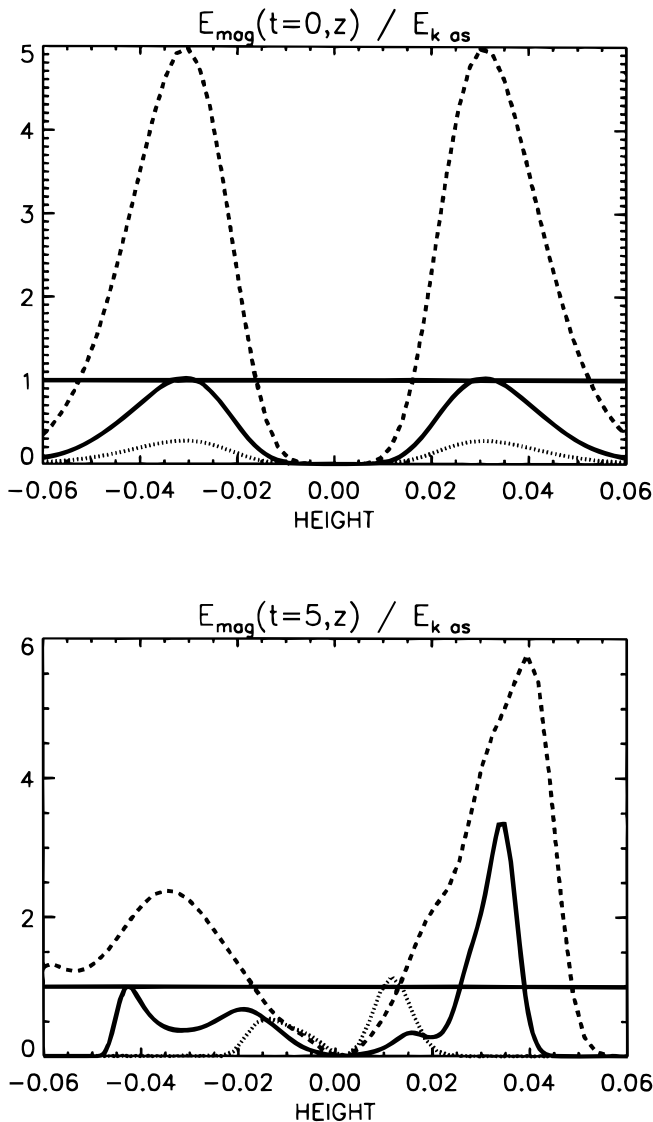


FIG. 16.—Initial and asymptotic profiles of the distribution of magnetic energy in the transverse field,  $e_{mag}$ , along the vertical axis of symmetry compared, in both cases, with the asymptotic kinetic energy density  $e_{kas}$  at the apex of the tube. The asymptotic values were calculated at  $t = 5$ . The different curves correspond to cases with initial pitch angle  $\Psi_{mt} = 13.9^\circ$  (dashed line),  $\Psi_{mt} = 7^\circ$  (solid line), and  $\Psi_{mt} = 2.5^\circ$  (dotted line).

results of Longcope et al. (1996).

Further insight into the structural differences of the tubes in Figure 14 can be obtained by comparing the energy density of the transverse field,  $e_{mag}$ , with the kinetic energy reached asymptotically by the head of the tube. The order of magnitude of the latter is  $(B_i^2/8\pi)\tilde{R}(1 + \tan^2 \Psi)$ . This varies little (about 6% only) between  $\Psi_{mt} = 2.5^\circ$  and  $\Psi_{mt} = 13.9^\circ$ . The magnetic energy of the transverse field, in contrast, varies by a large factor (approximately 30) between those two extremes. For the comparison in Figure 16, we plot the distribution of  $e_{mag}$  along the vertical axis at times  $t = 0$  (upper panel) and  $t = 5$  (lower panel), divided in both cases by the kinetic energy density at the upper stagnation point of the tube in the asymptotic regime,  $e_{kas}$  (calculated in the figure at time  $t = 5$ ). In the case with the highest  $\Psi_{mt}$  (dashed line), at  $t = 0$  only a thin skin at the outermost tube boundary is below the terminal kinetic energy level; we expect a skin of roughly that size to be dragged into the wake. For  $\Psi_{mt} = 7^\circ$  (solid line) and  $\Psi_{mt} = 2.5^\circ$  (dotted line), most (or all) of the tube at time  $t = 0$  has  $e_{mag}$  below the  $e_{kas}$  level. However, in the initial phases of the evolution, the transverse field is substantially intensified through the compression and stretching phenomena explained in § 4. This allows the head of the tube to be formed and its energy  $e_{mag}$  to be at (or above) the  $e_{kas}$  level in the asymptotic regime (Fig. 16, dotted line in second plot).

## 8. DISCUSSION

The results presented in this paper can be discussed from a twofold perspective. First, they can be applied to the theory of magnetic activity in the Sun, in trying to understand different aspects of the rise of magnetic flux across the convection zone. On the other hand, the simulations described here bear a strong resemblance to the results of laboratory and numerical experiments on the motion of air bubbles and rigid cylinders; it would be as well to clarify similarities and differences. The following subsections discuss different aspects of those topics.

### 8.1. The Parameters and Distribution of Basic Physical Variables

The numerical calculations of the present paper are necessarily idealized. The calculations were done in a high- $\beta$  regime with a small ratio of radius to pressure scale height. In this, they are within the parameter regime expected for the magnetic tubes in the deep convection zone. The latter have a larger  $\beta$ , by a factor between 10 and 100, than adopted here, but many qualitative features of the rise should be similar in both cases. The only diffusive process considered, however, the ohmic resistivity, taken together with the numerical viscosity and diffusion, yields laminar flows in and around the tube with a Reynolds number of a few hundred. This cannot be expected to hold in the actual Sun, where the rise of the tube will be accompanied by turbulent flows (with, in particular, a turbulent wake).

In spite of the above considerations, one conclusion seems unavoidable: for the transport of the magnetic flux to the surface in the form of buoyant magnetic flux tubes to be effective, the latter must be twisted from the early stages of their rise. We have shown that for a tube with a density deficit on the order of the full isothermal value ( $\Delta\rho/\rho \sim$

$-1/\beta$ ), an average pitch angle of around  $\sin^{-1} [(R/H_p)^{1/2}]$  is indeed necessary for the tube to withstand the various deforming agents. Otherwise, they lose most of their magnetic flux to the trailing wake. As shown by earlier authors, the vortex rolls of the wake can easily end up moving horizontally rather than rising. The condition on the minimum pitch angle may be less stringent, however, if we consider that the rise may actually be driven by the Parker instability in tubes that are stored in a neutrally buoyant equilibrium (Caligari, Moreno-Insertis, & Schüssler 1995). The instability occurs with the upgoing mass elements being driven by a vertical force that remains well below  $\rho g/\beta$  while the amplitude is not too large. Through equation (11), corresponding to a driving force of  $f\rho g/\beta$  ( $f \ll 1$ ) is a minimum pitch angle that is about a factor of  $f^{1/2}$  smaller than for isothermal straight tubes. For example, in the case discussed by Caligari et al. (1995),  $f < 0.04$  for the top of the rising loop in the lowermost 10,000 km of the rise, i.e., for distances equivalent to about 5 times the tube radius.

Even if the tubes are strongly buoyant [ $|\Delta\rho/\rho| = O(1/\beta)$ ] from the beginning, their time evolution may depend to some extent on the precise distribution of the density deficit in the tube at time  $t = 0$ . A Gaussian profile, as used in this paper, yields a fast deformation of the initial magnetic configuration, followed by internal torsional oscillations. This is directly associated with the torque of the buoyancy force throughout the tube interior. A top-hat profile ( $\rho_i < \rho_e$ , but  $\Delta\rho = \text{const}$ ), on the other hand, has no buoyancy torques associated with it except at the tube boundary. Yet, the time evolution of such a tube for smooth pitch angle distributions, such as those of equations (8) or (9), is qualitatively similar to the cases studied in this paper, as has been tested through a series of numerical experiments. This can be understood in different ways: first, the hydrodynamic forces associated with the external flow depend on the speed of rise of the tube, which is a function of the average buoyancy rather than of the precise shape of the  $\Delta\rho$  profile. To counteract them, one needs to have a sufficient pitch angle in the tube interior. On the other hand, the gravitational term in the vorticity equation (14) for a top-hat profile is concentrated at the periphery of the  $\Delta\rho$  distribution, but is correspondingly more intense. To counteract it, it is necessary to have a large current density  $J_i$ , which can only be achieved if  $B_i$  is sufficiently intense, at least close to the tube boundary. Through both arguments, one arrives at criteria basically similar to equation (11).

## 8.2. Twisted Tubes in the Convection Zone: Three-dimensional Effects

If the magnetic tubes that yield active regions at the surface must be twisted already in the early stages of the rise, the Sun should have a mechanism to routinely produce twisted tubes in the dynamo layers. If one relaxes the condition of symmetry along the tube imposed in the present paper, one might think that the twist could result through torsional shearing. This might come about as a natural sub-product of the generation of vorticity explained in this paper, if it took place at different rates on the different cross sections of the tube along the axis. This can be the case, for instance, if the originally horizontal tube develops an omega-loop shape in which a stretch of it rises while the rest remains at the original level. If the tube was originally untwisted (or only weakly twisted), the rising sections would tend to turn into vortex tube pairs that contain most of the

original magnetic flux. Now, in contrast to the two-dimensional case, this rotation produces a transverse field component in the flanks of the rising section of the loop. If enough  $B_t$  is built up, the rotation in the vortices could be braked. Yet, a simple calculation shows that for this mechanism to be at all effective, the footpoint separation,  $\lambda$ , of the omega loop must be small—in fact, smaller than one pressure scale height. More precisely, if we require that the tube develop a transverse component of the level required by the criterion of equation (11) after rising a distance equivalent to a few of its own radii, we obtain

$$\frac{\lambda}{H_p} \lesssim \left(\frac{R}{H_p}\right)^{1/2}. \quad (28)$$

This is a very small footpoint separation; the ratio of the Lorentz force associated with the curvature of the field lines to the buoyancy force in such a tube is at least of order  $H_p/\lambda$ . Consequently, it is not easy to raise a loop that is narrow enough for a sufficient pitch angle to develop at all. This is an indication that the tubes may need to be formed with the necessary amount of twist before they start to rise.

An interesting possibility for generating magnetic tubes with a nonzero total twist has been discussed by Cattaneo, Chiueh, & Hughes (1990); they consider a Rayleigh-Taylor unstable slab of plasma with a horizontal magnetic field such that the angle subtended by the field vector with a fixed horizontal axis monotonically changes with depth. Upon development of the instability, the layer yields magnetic tubes with nonzero degrees of twist. In their experiment, the authors showed how the resulting tubes were more resistant to deformation through the surrounding flows than in corresponding untwisted cases (Cattaneo & Hughes 1988). A corresponding three-dimensional problem has been calculated by Matthews, Hughes, & Proctor (1995). They show how an unstable layer with a parallel horizontal field produces magnetic tubes with nonzero vorticity. Through nonlinear interaction, these tubes arch as they rise in a vertical plane, thereby becoming twisted.

Another open question concerns the fate of a twisted tube as it rises across successive density scale heights in the convection zone. The internal and external densities are essentially equal for most of the rise (except for the small relative difference, on the order of up to  $1/\beta \ll 1$ ); the tube thus expands, and its field intensity weakens by several orders of magnitude along the journey (see Moreno-Insertis 1986, 1992, 1997b). In fact, the beginning of this process can be seen by comparing the maximum field intensity of the three panels of Figure 8. The rate of decrease associated with an off-axis expansion of the tube, however, is different for the longitudinal and transverse components of the field (see Parker 1979, § 9). A rough but simple argument based on the conservation of flux in two dimensions yields a rate of change of the twist that follows an approximate law,  $\tan \Psi \propto R$ . If this holds, the tubes could reach the upper convection zone with very large degrees of twist, possibly such that they can become kink-unstable. Yet, three-dimensional effects could render that simple law of little use. The stretching of the tube apex in the longitudinal direction, for instance, a phenomenon common in Parker unstable rising loops, may reduce the level of twist there. Also, the conservation of the total helicity in the tube could put an upper limit to the number of turns in the field lines around the axis at any single point. However it is, large pitch angles

should be a common feature in rising tubes when they reach photospheric levels. The sheared field structures observed in emerging active regions (Lites et al. 1995; Leka et al. 1996) may be a consequence of this (see also Tanaka 1991; Kurokawa 1989; Rust & Kumar 1996).

### 8.3. Magnetic Tubes, Air Bubbles, and Rigid Cylinders: Similarities and Differences

Throughout this paper we have compared our results to the laboratory experiments of flow past rigid cylinders and air bubbles at  $Re \simeq 200\text{--}300$ . We here summarize the similarities and differences found.

1. *Magnetic tubes and air bubbles.*—Remarkable similarities were found in (1) the general shape and structural features (skirt, central tail) and (2) the *protection* of the interior of the rising object through surface tension. These similarities are all the more striking given the difference in buoyancy [density deficit  $|\Delta\rho/\rho| \ll 1$  for tubes,  $O(1)$  for bubbles] and in the physical source of the surface tension (capillary effects versus jump in the tangential field component). As a result, defining the Weber number on the basis of the corresponding surface tension mechanism, one can formulate a common law of dependence of structural properties on  $We$ .

2. *Magnetic tubes and rigid cylinders.*—A clear similarity is evident in the boundary layers; both objects have a no-slip condition along the boundary. Consequently, the relative jump of the tangential velocity across the boundary layer is large,  $[v_{tg}]/v_{tg} \sim O(1)$ . In contrast, there is a zero tangential stress condition along the fluid/air interface of a bubble; correspondingly,  $[v_{tg}]/v_{tg} \sim O(Re^{-1/2})$ . As a result

of the no-slip condition, both buoyant magnetic tubes and rigid cylinders produce (and shed downstream) secondary rolls near the point of separation of the boundary layer.

3. *Features specific to the buoyant magnetic tubes with twist.* In the magnetic tubes of the present simulations, the wake is formed in the initial phases of the rise out of material bodily transported from the initial tube. Thus, the wake is magnetized and maintains a magnetic connection to the head of the rising tube along time. The behavior of the magnetic rope depends directly on the amount of magnetic flux incorporated into the wake, which, in turn, depends on the initial twist. In the case of an initially highly twisted tube ( $\Psi_{mt} = 13^\circ 9$ ), the magnetic rope is almost rigid and its shape and the flow around it strongly resemble those of a solid cylinder. If the initial pitch angle is closer to the threshold of equation (11), then the tube deforms and adopts a *bubble-like* shape (although it still satisfies a no-slip condition along its boundary). Finally, if  $\Psi_{mt}$  is very small, the tube behaves like a rising *thermal* (Longcope et al. 1996).

This work was partially funded through the DGES project No. 95-0028-C of the Spanish Ministry of Education and Culture. The numerical calculations were carried out using the computing resources of the Instituto de Astrofísica de Canarias and of the Centre de Computació i Comunicacions de Catalunya. The authors are grateful to Doctors M. Kaisig and K. Shibata for providing the numerical code and for their subsequent help with it. Thanks are also due to a large number of scientists at HAO, JILA, and CORA in Boulder (Colorado) as well as at the University of Chicago for illuminating conversations on the topic of this paper.

### REFERENCES

- Batchelor, G. K. 1967, *An Introduction to Fluid Dynamics* (Cambridge: Cambridge Univ. Press)
- Bouard, R., & Coutanceau, M. 1980, *J. Fluid Mech.*, 101, 583
- Caligari, P., Moreno-Insertis, F., & Schüssler, M. 1995, *ApJ*, 441, 886
- Cargill, P. J., Chen, J., Spicer, D. S., & Zalesak, S. T. 1996, *J. Geophys. Res.*, 101, 4855
- Cattaneo, F., & Hughes, D. W. 1988, *J. Fluid Mech.*, 196, 323
- Cattaneo, F., Chiueh, T., & Hughes, D. W. 1990, *J. Fluid Mech.*, 219, 1
- Collins, R. 1965, *Chem. Eng. Sci.*, 20, 851
- Collins, W. M., & Dennis, S. C. R. 1973a, *Q. J. Mech. Appl. Math.*, 26, 53
- , 1973b, *J. Fluid Mech.*, 60, 105
- Choudhuri, A. R. 1989, *Sol. Phys.*, 123, 217
- Christov, C. I., & Volkov, P. K. 1985, *J. Fluid Mech.*, 158, 341
- Dandy, D. S., & Leal, L. G. 1989, *J. Fluid Mech.*, 208, 161
- Davies, R. M., & Taylor, G. I., *Proc. R. Soc. London A*, 200, 375
- D'Silva, S., & Choudhuri, A. R. 1993, *A&A*, 272, 621
- Emonet, T., & Moreno-Insertis, F. 1996, *ApJ*, 458, 783
- Fan, Y., Fisher, G. H., & DeLuca E. E. 1993, *ApJ*, 405, 390
- Fan, Y., Fisher, G. H., & McClymont, A. N. 1994, *ApJ*, 436, 907
- Fan, Y., Zweibel, E. G., & Lantz, S. R. 1997, *ApJ*, 493, in press
- Hnat, J. G., & Buckmaster, J. D. 1976, *Phys. Fluids*, 19, 182
- Hughes, D. W., Falle, S. A. E. G., & Joarder, P. 1998, *MNRAS*, submitted
- Kaisig, M., Tajima, T., Shibata, K., Nozawa, S., & Matsumoto, R. 1990, *ApJ*, 358, 698
- Kurokawa, H. 1989, *Space Sci. Rev.*, 51, 49
- Leka, K. D., Canfield, R. C., McClymont, A. N., & van Driel-Gesztelyi, L. 1996, *ApJ*, 462, 547
- Lites, B. W., Low, B. C., Martínez Pillet, V., Seagraves, P., & Skumanich, A. 1995, *ApJ*, 446, 877
- Longcope, D. W., Fisher, G. H., & Arendt, S. 1996, *ApJ*, 464, 999
- Matthews, P. C., Hughes, D. W., Proctor, M. R. E. 1995, *ApJ*, 448, 938
- Moreno-Insertis, F. 1983, *A&A*, 122, 241
- , 1986, *A&A*, 166, 291
- , 1992, in *Sunspots, Theory and Observations*, ed. J. H. Thomas & N. O. Weiss (Dordrecht: Kluwer), 385
- , 1997a, in *The Inconstant Sun*, ed. C. Marmolino & G. Cauzzi, *Mem. Soc. Astron. Italiana*, 68
- , 1997b, in *Solar Magnetic Fields*, ed. Viggo Hansteen (Oslo: Univ. Oslo), 3
- Moreno-Insertis, F., & Emonet, T. 1996, *ApJ*, 472, L53
- Nordlund, Å., & Stein, R. F. 1990, *Comput. Phys. Commun.*, 59, 119
- Parlange, J.-Y. 1969, *J. Fluid Mech.*, 37, 257
- Parker, E. N. 1979, *Cosmical Magnetic Fields* (Oxford: Oxford Univ. Press), Chap. 9
- Richtmyer, R. O., & Morton, K. W. 1967, *Difference Methods for Initial-Value Problems* (2d ed.; New York: Interscience), Chap. 13
- Rubin, E. L., & Burstein, S. Z. 1967, *J. Comp. Phys.*, 2, 178
- Rust, D. M., & Kumar, A. 1996, *ApJ*, 464, L199
- Ryskin, G., & Leal, L. G. 1984a, *J. Fluid Mech.*, 148, 1
- , 1984b, *J. Fluid Mech.*, 148, 19
- Schüssler, M. 1979, *A&A*, 71, 79
- Shibata, K. 1983, *PASJ*, 35, 263
- Shibata, K., Tajima, T., Steinolfson, R. S., & Matsumoto, R. 1989, *ApJ*, 345, 584
- Stone, H. A. 1994, *Annu. Rev. Fluid Mech.*, 26, 65
- Ta Phuoc Loc. 1980, *J. Fluid Mech.*, 100, 111
- Ta Phuoc Loc, & Bouard, R. 1985, *J. Fluid Mech.*, 160, 93
- Tanaka, K. 1991, *Sol. Phys.*, 136, 37
- Tsiganos, K. C. 1980, *ApJ*, 239, 746
- Wegener, P. P., & Parlange, J.-Y. 1973, *Annu. Rev. Fluid Mech.*, 5, 79